

INVESTIGATION OF PHYSICAL PROPERTIES OF PYROCHLORE IRIDATES

A thesis submitted towards the partial fulfilment of BS-MS Dual
Degree Programme

by

KSHITI MISHRA

Under the guidance of

DR. SURJEET SINGH



INDIAN INSTITUTE OF SCIENCE EDUCATION AND RESEARCH

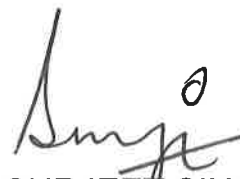
(IISER), PUNE

Certificate

This is to certify that this thesis titled 'INVESTIGATION OF PHYSICAL PROPERTIES OF PYROCHLORE IRIDATES' submitted towards the partial fulfilment of the BS-MS Dual Degree Programme at the Indian Institute of Science Education and Research, Pune represents original research carried out by KSHITI MISHRA at IISER Pune, under the supervision of DR. SURJEET SINGH during the academic year 2014-2015.



KSHITI MISHRA



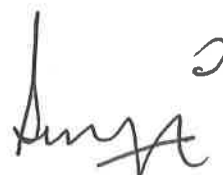
DR. SURJEET SINGH

Declaration

I hereby declare that the matter embodied in the report titled 'INVESTIGATION OF PHYSICAL PROPERTIES OF PYROCHLORE IRIDATES' are the results of the investigations carried out by me at the Department of Physics, IISER-Pune under the supervision of Dr. Surjeet Singh, and the same has not been submitted elsewhere for any other degree.



KSHITI MISHRA



DR. SURJEET SINGH

Acknowledgements

I thank my supervisor Dr. Surjeet Singh for giving me the chance to work on this project, and for his guidance, support and encouragement at every stage of it. His immense enthusiasm for Physics has always been a source of inspiration and working under his guidance has been a most enriching learning experience.

I would also like to thank our lab group – Koushik Karmakar, Rabindranath Bag, Prachi Telang, Rohit Kumar, and Vinayak Kulkarni – for all the fun, the discussions and the *chai*, which proved to be essential factors for lab productivity! Koushik bhaiya and Rabindranath bhaiya, thank you for always being there for any sort of guidance, useful discussion and crisis management. Moments spent with Prachi discussing Physics, movie plots, and other worldly things will forever be treasured. Tea breaks with my lab-mates, and Shreya, Charu and Shanu need to be acknowledged for the timely and much-needed energy boosts that they were. I am also grateful to all the technical staff at h-cross Block for their help with a lot of the measurements that form an important part of this thesis.

I would like to express my most sincere gratitude to IISER Pune for providing us with such a wonderful atmosphere for nurturing scientific thought, the chance to interact with knowledgeable and enthusiastic faculty, and the luxury of so many opportunities and facilities. Thanks are also due to KVPY for providing sustenance in the form of monthly stipends!

I must thank my friends – a couple of the finest Nehas (out of the very many!), and Aashay, Pranav, Anurag, Sharath, for meal-time reminders, trouble-sharing, Saturday night dinners, quizzing, financial aid, and everything else that drove me through the past year; Krishna, Krithika and Raag for letters and long e-mails to lift drooping spirits; Meghana, Niharika, Ashwini, Leshu, Sumanth, Mounika, Snigdha, Rini, Shivani, Prithvijit and Dhaval for all the conversations and life-talk, long and short, on the phone and off it; and ALL the amazing people in my batch - you are all too many to name - for making my five years here the best they could have been.

I also want to express my deepest and most sincere gratitude to my parents and my brother, for being the best support system I could ever have had, at all times, and for their unconditional and immense love and patience.

Abstract

This study aims to investigate materials belonging to the pyrochlore iridate family – a class of materials with the formula $A_2Ir_2O_7$ (A – trivalent ion). These materials have been the focus of a lot of research in Condensed Matter Physics because several factors such as electronic correlations, crystal fields, a geometrically frustrated lattice and spin orbit coupling act on these systems to give rise to novel behaviour. Exotic electronic ground states have been predicted to arise in these compounds as a result of the above-mentioned interplay of interactions. One of the most interesting feature displayed by these compounds is a coupled metal-to-insulator and magnetic transition, which is not very well understood. Insight into the mechanism of this transition could yield information about electronic behaviour in the presence of large spin-orbit coupling. However, it is difficult to probe into the system directly through neutron scattering because of the large neutron absorption cross section of Ir^{4+} . Hence other methods of studying a system's behaviour have to be resorted to.

In this study, perturbation by chemical doping has been used to study the behaviour of two iridates $Eu_2Ir_2O_7$ and $Bi_2Ir_2O_7$ by synthesising compounds having intermediate compositions, and studying the physical properties of the resulting series.

Both the samples individually display very different behaviour despite having a similar structure and non-magnetic ions on the A-site. $Eu_2Ir_2O_7$ displays a metal-insulator transition at 120K accompanied by a magnetic transition into a long range ordered phase. $Bi_2Ir_2O_7$, on the other hand, is metallic down to very low temperatures and also doesn't show any magnetic ordering. This study aims to investigate the transition between the behaviours seen in these two compounds belonging to the same family.

Compounds with 5, 10, 25, 50 and 75% Bismuth doping in $Eu_2Ir_2O_7$ and $Bi_2Ir_2O_7$ were prepared by solid state synthesis. After performing structural and compositional characterisation, their magnetic properties and electron transport properties were studied to observe how the behaviour changed across the series. The observed behavioural trends have been described in the thesis.

Contents

Introduction	7
The Pyrochlore Structure	12
Magnetism and Interactions in the Iridates	13
Magnetism in Solids.....	13
Geometrical Frustration.....	17
Interactions	19
Summary	22
Experimental Techniques	23
Sample Synthesis	23
Sample Characterisation.....	24
X-Ray Diffraction.....	24
Scanning Electron Microscopy and Energy Dispersive Spectroscopy	25
Measurement of Physical Properties.....	27
The Physical Property Measurement System.....	27
Transport Property Measurements.....	28
Magnetic Property Measurements.....	31
Heat Capacity Measurements	33
Results and Discussion	34
Structural Characterisation.....	34
Microstructure and Composition.....	39
Magnetic Measurements.....	43
Electrical Transport Measurements.....	57
Effect of Off-Stoichiometry in $\text{Eu}_2\text{Ir}_2\text{O}_7$	61
Conclusions and Outlook	63
Bibliography	65

Chapter 1

Introduction

Transition metal oxides (TMOs) are a widely-studied class of materials in Condensed Matter Physics and Materials Science because of their interesting physical properties and variety of potential applications. The phenomena that are of particular interest to condensed matter physicists include high-temperature superconductivity, colossal magnetoresistance, multiferroicity, spin dependent transport (spintronics), geometrical frustration and a variety of magnetic ground states that the TMOs are known to exhibit. These properties primarily arise due to the d-electrons associated with the transition metal ions [1] [2]. TMOs crystallise in a wide range of structures. Among these, the pyrochlore family of TMOs represents a class of compounds with chemical formula $A_2B_2O_7$ where the cations A and B can be chosen from a wide range of combinations. This class gets its name due to its structural similarity to the mineral, pyrochlore $\text{NaCaNb}_2\text{O}_6\text{F}$ [1]. Here, we shall focus on the pyrochlores with the valence combination +3, +4, i.e., $A_2^{3+}B_2^{4+}O_7$. Some of the widely studied examples of such pyrochlores include rare-earth titanates ($A_2\text{Ti}_2\text{O}_7$), zirconates ($A_2\text{Zr}_2\text{O}_7$), molybdates ($A_2\text{Mo}_2\text{O}_7$) and iridates ($A_2\text{Ir}_2\text{O}_7$). In most cases, A is a rare-earth ion. It must, however, be pointed out here that within these sub-families, the choice of the A ion is limited by the field-of-stability of the pyrochlore structure, which is determined by the ratio of the ionic radii of the two cations: for example, $\text{La}_2\text{Zr}_2\text{O}_7$ has the pyrochlore structure but $\text{La}_2\text{Ti}_2\text{O}_7$ does not, whereas $\text{Tb}_2\text{Ti}_2\text{O}_7$ has the pyrochlore structure but $\text{Tb}_2\text{Zr}_2\text{O}_7$ crystallises with a defect-flourite structure. These points are discussed in detail under the section 'Structural Details'. We shall refer to a compound with $A_2B_2O_7$ as 'magnetic pyrochlore' if either of A or B or both are magnetic. For example, $\text{Tb}_2\text{Ti}_2\text{O}_7$ is a magnetic pyrochlore where as $\text{Lu}_2\text{Ti}_2\text{O}_7$ is a 'non-magnetic' pyrochlore, since Tb^{3+} with 8 f-electrons has a non-zero magnetic moment in its ground state; while Lu^{3+} , having 14-f electrons, does not have a permanent magnetic moment. Note that in both cases the Ti^{4+} (d^0 -ion) is 'non-magnetic'. In $\text{Tb}_2\text{Ir}_2\text{O}_7$, on the other hand, both A and B-sites are magnetic.

Magnetic pyrochlores exhibit the phenomenon of *geometrical frustration*. Briefly, geometrically frustrated materials are characterised by an inability to stabilise in a unique magnetic ground state because of an apparent incompatibility between the spin-spin interactions and the underlying crystalline symmetry. In the pyrochlores, for example, A and B ions form interpenetrating networks of corner-linked tetrahedrons which is one of the most frustrated lattice geometry in three-dimensions. Magnetic Pyrochlores, therefore, display a wide range of unconventional magnetic ground states that are attributed to their frustrated nature. These include the spin-glass like magnetic ground state of $\text{Y}_2\text{Mo}_2\text{O}_7$, spin liquid ground state of $\text{Tb}_2\text{Ti}_2\text{O}_7$ down to a temperature of 70 mK, spin ice ground state of $\text{Dy}_2\text{Ti}_2\text{O}_7$, $\text{Ho}_2\text{Ti}_2\text{O}_7$ and

$\text{Nd}_2\text{Mo}_2\text{O}_7$, superconducting ground state of $\text{Cd}_2\text{Re}_2\text{O}_7$, anomalous Hall effect of $\text{Nd}_2\text{Mo}_2\text{O}_7$ and the heavy Fermion behavior of $\text{Pr}_2\text{Ir}_2\text{O}_7$. (For a review, see [1])

A sub-family among the pyrochlores is that of Iridates, where the B-site in $\text{A}_2\text{B}_2\text{O}_7$ is occupied by Iridium (Ir^{4+}). Pyrochlore iridates are considered promising candidates for the experimental realisation of exotic phases of matter such as Spin Liquids, Topological Semimetals and Weyl Semi-metals [3][4]. Their potential to host such phases comes from the competing energy scales of spin-orbit coupling, crystal field effects and electronic correlations on a geometrically frustrated lattice. These phases, if realised experimentally, could prove useful in the fields of quantum computation and spintronics, revolutionising information storage and data processing [3][5][6]. At the fundamental level, these materials are a great platform to study the behaviour that emerges when usually weak interactions become strong enough to act on comparable energy scales. While research in quantum condensed matter until very recently focussed on understanding and exploiting the consequences of strong electronic correlations, the iridates provide a rare opportunity of exploring the physics of materials where spin-orbit interaction energy competes with that of the electron-electron interactions.

Because of these prospects, several experimental and theoretical studies have tried to analyse the behaviour of pyrochlore iridates. Most of these studies were aimed at studying the contribution of the Iridium 5d electrons to the magnetic and electrical properties of these pyrochlores. In this regard, the pyrochlores with non-magnetic A-site ion, such as, $\text{Eu}_2\text{Ir}_2\text{O}_7$, $\text{Y}_2\text{Ir}_2\text{O}_7$ and $\text{Bi}_2\text{Ir}_2\text{O}_7$ are important - they could provide useful insights into the physics of Ir^{4+} electrons in their ensuing physical properties, since they show interesting magnetic behavior arising solely from the Ir 5d electrons. In general, many iridate pyrochlores with A-site substituted with different ions have been investigated. Popular candidates for the A-site substitution are rare-earth ions (the series from Lanthanum to Lutetium, and Yttrium) since these have stable ions in the 3+ oxidation state, and show a regular variation in their ionic sizes because of lanthanide contraction [7].

The results of these studies imply that the A-site ions (independent of their magnetic moment) also have some role to play in the ground state assumed by the pyrochlore Iridates. One of the trends observed is that as the radius of the A-site ion increases, the ground state becomes increasingly metallic [8]. For instance, $\text{Pr}_2\text{Ir}_2\text{O}_7$ shows a metallic resistivity down to the lowest temperatures, whereas $\text{Tb}_2\text{Ir}_2\text{O}_7$ along with other heavier rare-earths exhibit an insulator like resistivity. The intermediate members, i.e., Nd, Sm and Eu show a metal – to – insulator transition (MIT) near $T = 36, 117$ and 120 K, respectively. This is summarised in the phase diagram in Fig. 1.1.

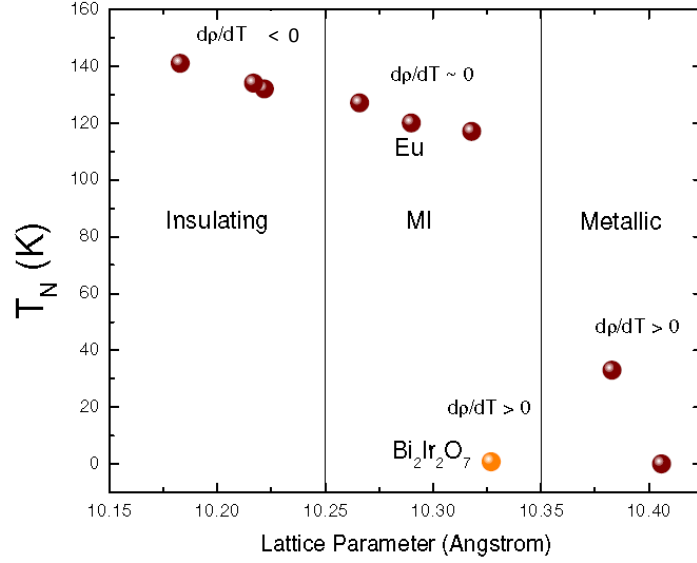


Fig 1.1 The phase diagram of the pyrochlore iridates showing the MIT across the series varying with unit cell parameter/A-site ionic radius

A more detailed summary of the variation of metallic behaviour with lattice parameter of the iridates and radius of the A-site ionic radius is given in the following table:

Table 1.1: Ionic radii of trivalent rare-earth ions in an eight-fold coordination and the lattice parameter of the corresponding iridate pyrochlores are shown to emphasise the regular variation of the unit-cell parameter across the series. The last two columns describe the nature of the ground state (metallic vs non-metallic and magnetically ordered vs no long-range spin order). For $\text{Bi}_2\text{Ir}_2\text{O}_7$, the corresponding parameters are shown in the shaded row. Note that despite having largest ionic radius, the unit cell of $\text{Bi}_2\text{Ir}_2\text{O}_7$ is smaller than that of the Pr and Nd pyrochlores.

A in $\text{A}_2\text{Ir}_2\text{O}_7$	A^{3+} ionic radius (A)	Lattice parameter (A)	T_{MIT} or T_N (K)	Sign of dp/dT
Ho^{3+}	1.015	10.183	-	NEG*
Dy^{3+}	1.027	10.217	140	NEG
Tb^{3+}	1.040	10.222	135	NEG
Gd^{3+}	1.053	10.266	130	NEG
Eu^{3+}	1.066	10.290	120	NEG < T_N < POS*
Sm^{3+}	1.079	10.318	117	NEG < T_N < POS
Bi^{3+}	1.170	10.327	0.08 ⁺	POS
Nd^{3+}	1.109	10.383	39	NEG < T_N < POS
Pr^{3+}	1.126	10.406		POS

+ Ref: [9] ; * NEG = Negative, POS = Positive; Ionic radii from ref. [10]; Lattice parameter ref. [7]

The MIT mentioned above is found to be accompanied by a difference in magnetic behavior under zero-field cooled (ZFC) and field cooled (FC) measurements, which marks the onset of magnetic ordering upon cooling [1][8][11]. In $\text{Pr}_2\text{Ir}_2\text{O}_7$, on the other hand, no magnetic ordering or the aforementioned ZFC-FC splitting has been seen. Muon spin relaxation [12] and theoretical calculations [2] have pointed to the existence of a state with long-range magnetic ordering below the MIT. However, the origin and nature of the transition is still unclear and, therefore, is the subject of numerous studies. For instance, if Ir^{4+} moments indeed undergo a long-range ordering, what is the reason for the huge thermomagnetic irreversibility (ZFC – FC splitting) observed in the absence of any magnetic hysteresis in the isothermal magnetisation? The problem is further augmented by the fact that the large neutron absorption cross section of Iridium makes it difficult to allow any definite conclusions about the presence or absence of magnetic long-range ordering [13]. Thus, in order to probe into the magnetism and the MIT of these materials, indirect methods need to be adopted such as perturbing the system using chemical composition, applied pressure, etc. and studying its response.

This thesis aims to study the compound $\text{Eu}_2\text{Ir}_2\text{O}_7$. Due to the electronic configuration of Eu^{3+} , its total angular momentum quantum number (J) in the Hund's derived ground state is 0 and hence it should have *no* net magnetic moment. The compound displays an MIT at $T \sim 120$ K, accompanied by ordering of the Ir^{4+} moments; the nature of ordering, however, is unknown as mentioned earlier. The transition to the ordered state seems to be very robust since it remains unaffected by applied magnetic fields as well as slight off-stoichiometry. [14]

We also investigated the pyrochlore $\text{Bi}_2\text{Ir}_2\text{O}_7$ where Bi^{3+} is non-magnetic. Relatively little work has been done on this compound. However, since its lattice parameters are within the range of the rare-earth iridates showing MIT, one would expect it to follow the trend and show a similar MIT and magnetic transition. But surprisingly, the compound remains metallic down to liquid Helium temperatures with no signs of magnetic ordering down to at least $T = 2$ K [15]. A recent muon spin relaxation study [9] indicates *two* magnetic transitions below $T = 2$ K, while another muon study done on the same compound [16] could not detect these transitions. One more recent study on flux grown single crystals suggests strongly Stoner enhanced Pauli paramagnetic ground state with a non-Fermi liquid resistivity behavior [17], a trait shown by strongly correlated systems showing Heavy Fermion Behaviour [18]. Both these papers have appeared very recently, clearly suggesting an increasing interest in understanding the unconventional metallic ground state of this compound.

A comparison of the properties of the Eu and the Bi pyrochlore iridates may shed light on the question of how the A site affects the properties of the iridates. Additionally, the MIT of $\text{Eu}_2\text{Ir}_2\text{O}_7$ can possibly be understood if one systematically destroys it by doping Bi^{3+} at the Eu^{3+} site.

This thesis consists of a study of physical properties of $\text{Eu}_2\text{Ir}_2\text{O}_7$ and $\text{Bi}_2\text{Ir}_2\text{O}_7$, and also of a series of compounds with intermediate compositions.

The rest of the thesis is organised as follows: we begin with an introduction to the pyrochlore structure and theoretical concepts relevant to the study, including the various interactions that drive the Iridates into behaving the way they do. Following this, the experimental techniques that were used to characterise the materials are described. The next chapter covers the results obtained, their analysis and discussion. The final part consists of conclusions drawn from the study and follow-up questions.

The Pyrochlore Structure

The Pyrochlore oxides get their name because of their structural similarity to the mineral called Pyrochlore ($\text{NaCaNb}_2\text{O}_6\text{F}$). Since it allows a wide variety of substitution of ions on its site, there exists a huge family of materials that crystallise with this structure. We restrict our focus to members of the family with the structural formula $\text{A}_2\text{B}_2\text{O}_7$, where A is a trivalent ion and B is a tetravalent transition metal ion.

The pyrochlore structure can be described in many different ways [7]. One of these descriptions, which is relevant to the problem addressed in the thesis, views the pyrochlore lattice as composed of interpenetrating lattices formed by A and B sublattices. These sublattices are composed of vertex-sharing tetrahedra of A and B ions as shown in Figure 2. Each ion sits at the vertex of two tetrahedra, giving rise to a *geometrical frustration*, the details of which are described later.

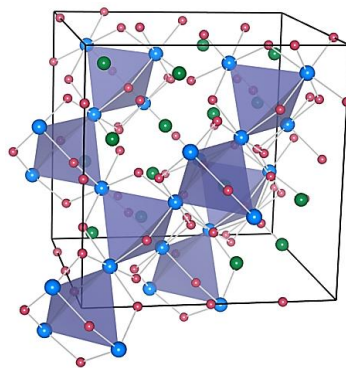


Fig 1.2 The pyrochlore structure seen as corner-sharing tetrahedra of Ir-ions. The rare earth ions are in green [29].

Another way of looking at the structure is to visualise it as composed of two types of polyhedra – The A ion is in 8-fold coordination i.e. surrounded by 8 oxygen ions, while the B ion is in 6-fold coordination (surrounded by 6 oxygen ions). The simplest polyhedron for the case of an ion in 8-fold coordination is a cube, while that for 6-fold coordination is an octahedron. However, in pyrochlores, the conditions for existence of a perfect cubic and perfect octahedral configuration cannot be satisfied simultaneously. One structural parameter – the oxygen position parameter, x – determines the shape of the polyhedron around the A and B ions.

Theoretically, the limiting values for x are from 0.3125 to 0.375. For $x = 0.3125$, the B ion is surrounded by a perfect octahedron, whereas the A ion is at the centre of a distorted polyhedron. In this coordination state, the A-ion is surrounded by a crown shaped ring comprising of six O atoms on the equatorial plane, and by two O atoms oriented along an axis

which is perpendicular to the plane of the crown. This is depicted in Figure 1.3. In some magnetic pyrochlores, it is this asymmetry which gives rise to Ising-like spins along the axial directions, giving rise to the spin-ice behaviour.

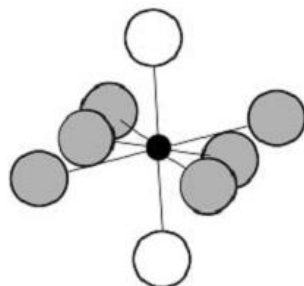


Fig 1.3 a. Coordination geometry of the A-site by O atoms [6]

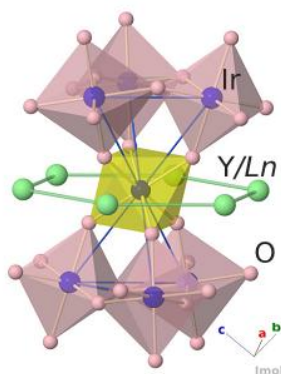


Fig 1.3 b. The octahedral coordination at the B-site (B = Ir, here) and its surrounding octahedra [19]

As the parameter x moves closer to 0.375, the polyhedron surrounding the B-ions becomes a distorted octahedron, while the polyhedron around A-ions starts to become more cubic. This description of the pyrochlore structure in terms of the oxygen position parameter could prove to be useful in the context of Iridates. A recent study of Iridates using X-Ray Absorption Spectroscopy [20] found that compounds with Ir^{4+} in an octahedral crystal field environment showed a high degree of spin-orbit coupling. Since the oxygen parameter can be correlated with the crystal field environment around the Ir-ion, one can investigate if it can be linked to the degree of spin-orbit coupling present in the Iridates as well.

Magnetism and Interactions in the Iridates

Magnetism in Solids

Magnetism in solids is a collective phenomenon that emerges due to the magnetic moments of individual atoms of the solid, which, in turn, arise due to the intrinsic magnetic moments of individual electrons in the atoms.

For an atom, which has multiple electrons, the total magnetic moment depends on the states occupied by the electrons. The electronic configuration having the minimum total energy is obtained when one follows a set of empirical rules known as Hund's Rules, which are:

1. Electrons should be arranged so as to maximise S . This prevents filling electrons with parallel spins in the same shell, minimising Coulomb repulsion.
2. The next step is to maximise L . This is based on the premise that electrons orbiting in the same direction can avoid each other more effectively, again lowering Coulomb repulsion.
3. The value of J can be obtained using $J = |L-S|$ if the shell is less than half full and $J = |L+S|$ if the shell is more than half full.

It must be noted that while the first two rules hold true always, the third rule is based on the assumption that the interaction between orbital and spin angular momenta, L and S , is weak compared to the electrostatic interactions between the electrons. In cases like the 3d transition metal compounds, this assumption fails because the interaction of the 3d electrons with their environment is no longer negligible compared to the Coulomb effects of individual atoms. For the rare-earth elements, however, their partially filled 4f-electrons are buried deep beneath the 5s/5p electrons which provide a protective shell from the surrounding crystalline environment. Thus, they obey the third Hund's rule quite well.

Now that we have a way of filling the electronic shells, we see that electrons pair up and occupy most of the shells completely, giving a net angular momentum of zero. Magnetism can be found only in those atoms which have partially filled shells with unpaired electrons.

Paramagnetism: Assuming that these unpaired electrons stay localised on their respective ion-cores, and that the magnetic moments on any arbitrarily chosen site do not interact with the magnetic moments on any other site of the lattice, then in the absence of a magnetic field, these moments point in random directions and there is no net magnetisation. Upon application of an external field, these moments tend to align in the direction of the field to minimise their magnetic potential energy. The extent of this alignment depends on the strength of the field and the temperature of the sample. While the field tends to line-up the moments, the effect of thermal energy is to randomise the orientations to maximise the entropy.

At any temperature T , the net magnetic moment per unit volume in the direction of the applied magnetic field is called the magnetisation, M , of the sample at that temperature. The magnetic susceptibility, χ , is defined as $\chi = M/H$ where H is the applied field strength. As is customary in literature, we shall use the CGS system of units, where the magnetic induction (B) in the sample is related to the applied field and the samples magnetisation using the relation: $B = 4\pi M + H$.

A statistical analysis of the energies and directions of the spins yields two important results concerning the magnetisation and the magnetic susceptibility of the sample:

The variation of the magnetisation of a paramagnetic system with the total angular momentum J , the applied field H , and temperature T , is given by the relation:

$$M = n g_J \mu_B J B_J(y)$$

Where n is the number of magnetic atoms, g_J is the Lande g -factor, a proportionality constant between a particle's angular momentum and its magnetic moment, μ_B is the Bohr magneton, which is a unit of expressing the magnetic moment of an atom ($1 \mu_B = 9.27 \times 10^{-24}$ J/T). $B_J(y)$ is the Brillouin function, which is a function of J , given by the expression:

$$B_J = \frac{2J+1}{2J} \coth\left(\frac{2J+1}{2J} y\right) - \frac{1}{2J} \coth\left(\frac{y}{2J}\right), \quad y = \frac{g_J \mu_B J H}{k_B T}$$

In the limit of small fields, the susceptibility obtained from the above expression comes out to be:

$$\chi = \frac{n \mu_0 \mu_{eff}^2}{3 k_B T},$$

where μ_0 is the permeability of the medium, μ_{eff} is the effective moment of the atom and k_B is the Boltzmann constant.

The inverse proportionality of the susceptibility to the temperature is known as the *Curie Law*. Thus, paramagnetic susceptibility plotted against temperature would look like a rectangular hyperbola, and the inverse of susceptibility plotted against temperature would yield a straight line with the slope C . These equations are useful while analysing experimentally obtained magnetic susceptibility data. [21]

When the interactions between the magnetic moments of a sample are non-zero, a long-range ordered state is established below a characteristic temperature known as Curie or Néel temperature depending on whether the interactions are ferromagnetic or antiferromagnetic. In such cases, it can be shown that the Curie law still remains valid above the ordering temperature, albeit with an important modification. The denominator in the original Curie law is replaced by $T - \theta_p$. The modified law is known as the Curie-Weiss law:

$$\chi = \frac{C}{T - \theta}$$

Here, C is the Curie constant, which is a measure of the effective magnetic moment of the sample, $k_B\theta_P$ (k_B is the Boltzmann constant) is the measure of the strength of interactions within the mean-field framework developed by Pierre-Ernest Weiss [6].

Thus, the presence of exchange interactions in a system is a necessity for attaining long range order. But not all systems with exchange interactions settle into an ordered state. There is a class of materials where an apparent incompatibility between the exchange interaction and the geometry of the underlying crystalline lattice tends to suppress the magnetic ordering to lower temperatures. This phenomenon is known as *geometrical frustration*, and will be described in a later part of this chapter.

van Vleck Paramagnetism: For most atoms of the lanthanide series, the total angular momentum states, or J levels corresponding to various energies lie very high above the ground state, and electrons at ordinary temperatures are unable to populate them. Therefore, the expression of the Curie-Weiss law discussed above works for the majority of them by considering the Zeeman splitting of the lowest or the ground J-multiplet. However, in some cases, such as Sm^{3+} and Eu^{3+} ions, these excited states are not so much higher in energy compared to the ground state. At room temperatures these states can still be populated and contribute to the total magnetic moment. This contribution of the excited energy levels to the magnetic moment is termed as *van Vleck paramagnetism*.

One of the compounds studied by us, $\text{Eu}_2\text{Ir}_2\text{O}_7$, has Eu in the +3 oxidation state. The electronic configuration of Eu^{3+} ($[\text{Xe}] 4f^6$) leads to a total $J = 0$, so the ground state doesn't contribute to the magnetism. However, Eu^{3+} still contributes to the magnetism of $\text{Eu}_2\text{Ir}_2\text{O}_7$ through its non-zero paramagnetism arising from the higher J-levels.

A statistically derived expression [22] which takes into account the various J multiplets due to spin-orbit coupling and the occupation-probability these levels as a function of the system temperature, gives the temperature dependence of the van Vleck susceptibility through the following equation:

$$\chi_{VV} = \frac{N\mu_B^2}{Z} \frac{A}{3\lambda}$$

where

$$A = (24 + \left(13.5 \frac{\lambda}{k_B T} - 1.5\right) e^{\frac{-\lambda}{k_B T}} + \left(67.5 \frac{\lambda}{k_B T} - 1.5\right) e^{\frac{-3\lambda}{k_B T}} + \left(189 \frac{\lambda}{k_B T} - 1.5\right) e^{\frac{-6\lambda}{k_B T}} + \left(405 \frac{\lambda}{k_B T} - 1.5\right) e^{\frac{-10\lambda}{k_B T}} + \left(742.5 \frac{\lambda}{k_B T} - 1.5\right) e^{\frac{-15\lambda}{k_B T}} + \left(1228.5 \frac{\lambda}{k_B T} - 1.5\right) e^{\frac{-21\lambda}{k_B T}}$$

and

$$Z = (1 + 3e^{\frac{-\lambda}{k_B T}} + 5e^{\frac{-3\lambda}{k_B T}} + 7e^{\frac{-6\lambda}{k_B T}} + 9e^{\frac{-10\lambda}{k_B T}} + 11e^{\frac{-15\lambda}{k_B T}} + 13e^{\frac{-21\lambda}{k_B T}})$$

Here, λ is the spin-orbit coupling constant which removes the $(2L + 1)(2S+1)$ degeneracy of the ground state, and is a measure of the energy difference between the ground state and the first excited state. The value of λ in terms of temperature for Eu^{3+} is different for different crystalline environments, and has been estimated to lie in the range of 400 – 500 K by several studies [14][23][24][25].

For a metal, there is also a magnetic contribution from the conduction electrons. This is referred to as the *Pauli paramagnetism*, and is found to be a weak, temperature independent susceptibility. This is because only those electrons close to the Fermi surface contribute to Pauli paramagnetism in metals, whereas for Curie paramagnetism, every atom of the material contributes. [21]

Geometrical Frustration

In very general terms, frustration arises when a system has competing or contradicting constraints, which cannot all be satisfied simultaneously to find a unique ground state [6][21]. When frustration arises as a consequence of the geometry of the lattice of a spin system, it is referred to as Geometrical Frustration. In the case of magnetic systems, the constraints are derived from the exchange interactions in the system.

To consider a very simple case, we take the example of a triangular lattice with spins on each vertex that interact antiferromagnetically. Suppose the spins are constrained to point either up or down (i.e., they are Ising-like spins), then as shown in the figure, after two adjacent spins are placed anti-parallel to each other, the third spin cannot simultaneously satisfy the criterion for antiferromagnetic alignment with both its neighbors, resulting in a state of frustration.

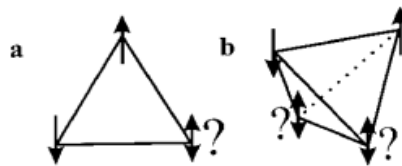


Fig 1.4 Geometric frustration on a triangular lattice and its 3-D analogue, a tetrahedral lattice [6]

In a single triangular motif with spins constrained to point only up/down there are two configurations of equal energy which can be attained. However, in a macroscopic lattice comprising of a large number of such triangles, the number of degenerate ground states the system can stabilise in also becomes macroscopic. If the frustration dominates down to $T = 0$ K, the system will show a finite spin entropy known as the residual entropy.

Magnetic materials in which magnetic moments lie on lattices of corner-sharing tetrahedra are even more frustrated. These are candidate materials for which exotic magnetic ground states can be expected [1]. The reason behind such a variety of complex spin structures and ground states has to do with the fact that at low enough temperatures, weak interactions that would not have been of any consequence in an unfrustrated system, begin to gain importance. One example of a weak interaction is the dipole-dipole interaction. In $\text{Dy}_2\text{Ti}_2\text{O}_7$, discussed below in more detail, a spin-ice ground state is obtained as a direct consequence of these dipolar interactions.

Despite the frustration at play, some systems do attain ‘compromise configurations’ which are non-collinear, but minimise the overall energy [6]. One such configuration is attained when on the triangular or tetrahedral motifs considered above, the spins are constrained to point towards or away from the body centre of the motif (rather than up/down as considered above). Such spins are locally Ising-like (i.e., the orientation of the Ising axis is different at different vertices of a structural motif). For a triangular lattice, the minimum energy configuration is one in which all three spins are aligned at 120° to each other (all pointing in or pointing out). For the case of the tetrahedron, such a configuration involves all spins pointing at 109° to each other. This is called an ‘all-in-all-out’ spin configuration, which is trivially degenerate (ground state degeneracy being 2). This example serves to explain how important the local anisotropies are in determining the ground state of a frustrated system.

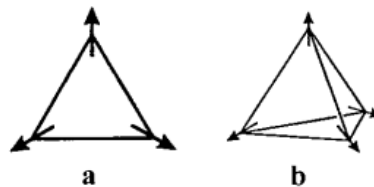


Fig 1.5 Compromise configurations for the triangular and tetrahedral lattices [6]

An interesting case of frustration on the pyrochlore lattice is shown by the pyrochlores $\text{Dy}_2\text{Ti}_2\text{O}_7$ and $\text{Ho}_2\text{Ti}_2\text{O}_7$ - crystal field interactions constrain the moments on each site to point either directly towards or away from the centres of the Dy/Ho tetrahedra [26][27]. The dipolar interactions (ferromagnetic) between neighboring spins cause the system to assume a two-in-two-out configuration, similar to the ordering of hydrogen atoms seen in water – ice. These systems are therefore named ‘spin ices’.

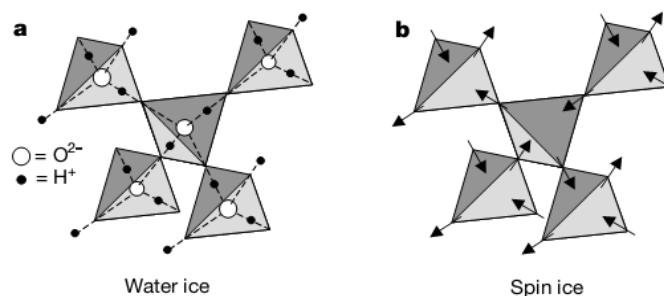


Fig 1.6 Spin Ice and Water Ice[27]

It has been proposed that the flipping of moments in these compounds due to thermal fluctuations can create effective separated magnetic monopoles [28].

There is also a possibility that a frustrated system might not be able to defy the generated quantum fluctuations to attain an ordered state even at low temperatures. This quantum disordered state is referred to as a spin liquid state, because the moments are constantly fluctuating like the molecules of an actual liquid [1]. Again, members of the pyrochlore family such as $Tb_2Ti_2O_7$ and probably $Pr_2Ir_2O_7$ [1] show such a phase.

Coming back to the context of the pyrochlore Iridates, most of them have been observed to attain an ordered phase at low temperatures, but the exact nature of this phase remains unclear. Muon spin relaxation results [12] have proposed that the ordered structure is most likely an “all-in-all-out” type. If this is established unequivocally, it might have important consequences regarding the ability of this state to support the proposed novel phases. However, the physics of the iridates is further complicated by the presence of several interactions, of which the dominant ones are described in the next section.

Interactions

Crystal Field Effects: In a crystalline solid, the crystal field around any ion on the lattice is the electric field generated by the ions surrounding it. [21] This crystal field affects the energies of the outermost orbitals of the atoms in ways that depend on its symmetry. The transition metal ion at the B-site in the pyrochlore lattice is octahedrally coordinated by the oxygen ions. Thus the crystal field due to the oxygen ions lifts the degeneracy of the five d-orbitals. In the simplest case of a regular octahedron, the orbitals $d_{x^2-y^2}$ and d_{z^2} (see fig. 1.7 below for the orientation of the coordinate axes) point towards the oxygen ions, which raises their electrostatic energy compared to d_{xy} , d_{yz} and d_{zx} . Therefore, in an octahedral crystal field the d-orbitals are split into a doublet (group theoretic notation: e_g) and a triplet (t_{2g}).

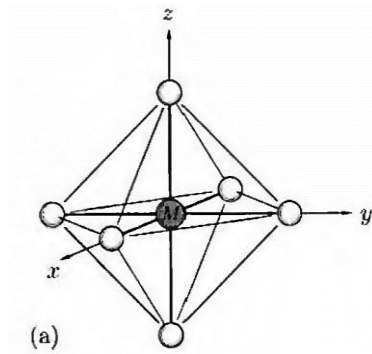


Fig 1.7 The octahedral crystal field environment around the B-site [21]

The magnitude of the splitting, Δ , relative to the energy required to pair up electrons in the same orbital determines whether the system will assume a high spin state (more unpaired electrons) or a low spin state (more paired up electrons). A high spin state would correspond to a higher magnetic moment.

The rare earth ions are also surrounded by oxygen ions, but their partially filled orbitals, which are the 4f orbitals, are buried deep beneath the protective shield provided by $5s^2$, $5p^6$ electrons and thus protected from the repulsive effects of the crystal field.

The effects of the crystal field increase as we go from 3d to 5d transition metal ions, since the orbitals become more spread out and thus more 'exposed' to the crystal field.

Electronic Correlation: Electronic correlation comes into the picture when itinerant electrons are present in a system. Due to the itinerancy of the electrons, the system should be conducting and the electrons should be delocalised over the entire crystal. They can hop from one site to another, provided that the final site is either empty, or occupied by a single electron with an antiparallel spin (due to Pauli's exclusion principle). But sometimes, the Coulomb repulsion on the lattice sites is too high so that the energy cost of filling one site with two electrons is enormous. Because of this, the movement of the electrons is no longer independent of each other – whether an electron 'hops' to a site or not depends on whether the site is already occupied. As the on-site Coulomb repulsion increases, the electrons become more localised and less metallic. In some cases, the electron correlation can be so high that the system acts like an insulator despite being predicted to be metallic by the band theory of solids. Such an insulator also tends to be antiferromagnetically ordered, because if an electron has a nearest neighbor with an antiparallel spin, it can briefly hop to the site lowering the kinetic energy of the system. A material which shows such a behavior is called a Mott Insulator. Examples of such insulators include transition metal oxides such as NiO, MnO, FeO, CoO, and La_2CuO_4 among others. When the on-site coulomb repulsion (U) is smaller

than the electronic bandwidth (W) the system can show metallic behavior. When U is comparable to W , metal-insulator transitions are observed. [21]

In a theoretical calculation of the energy of these electrons using the Hartree – Fock approximation (which assumes the electrons to be moving in an average field created by the other electrons), it is assumed that the motion of the electrons is independent of each other. This is why the Hartree-Fock energies obtained for Mott insulators differ from the actual energies by some amount. This difference is called correlation energy. For Mott insulators with very high U , the correlation energy will tend to be larger, because the electrons have a larger dependence on the presence of other electrons on a hopping site. The correlation energy in some sense is a measure of the on-site Coulomb repulsion, U . Systems with high U are said to be *strongly correlated systems*. Electronic correlation decreases as one goes from 3d to 5d transition metal ions. This is because the 5d orbitals are much more diffuse compared to 3d orbitals, allowing better overlap.

Spin-Orbit Coupling: Spin-orbit coupling, as the name suggests, is an interaction between the spin of an electron and its orbital motion around the nucleus. This motion generates a magnetic field that the spin interacts with electromagnetically. This alters the energy levels of the electron. The spin-orbit interaction energy is proportional to Z^4 . For elements with lower atomic numbers, this coupling is treated as a weak perturbation while obtaining the electronic energy levels. In such calculations, it merely causes the levels to split, giving fine structure levels corresponding to different J values. But for larger elements, such as Iridium, the spin-orbit coupling is no longer small enough to be treated as a perturbation. Because of this effect, the spin and orbital angular momentum of each electron are coupled separately first to give j -values, and then the relatively weaker electrostatic effect acts to couple the j values from each electron. [21]

The Case of the Iridates: For the Iridates, the three interactions described above act at comparable energy scales. The electronic correlation is of the order of 0.5 – 3 eV, the crystal field effects are about 1 – 5 eV, and the energy scale for spin-orbit coupling is 0.1 – 1 eV [20]. None of these can be treated as perturbations. The novel phases exhibited by so many of these Iridates are the result of this interplay between interactions, and are an excellent platform to study the same. The following phase diagram, adapted from [29] shows where Iridates lie regarding the relative strengths of correlations and spin-orbit coupling.

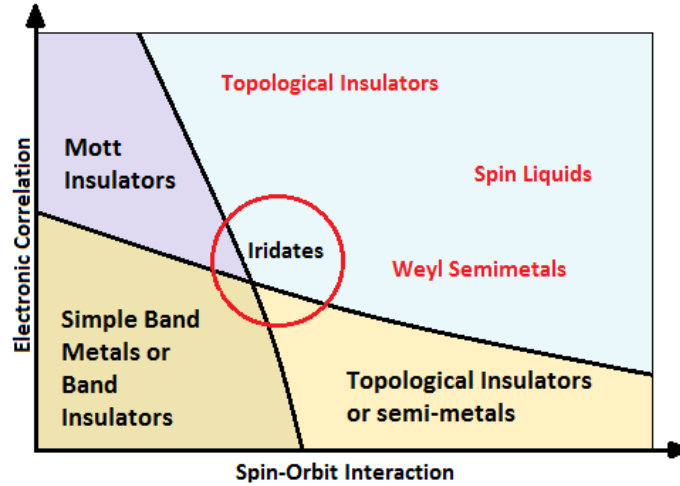


Fig 1.8 Phase diagram in terms of interaction strengths

The band theory of metals predicts that compounds containing the Ir^{4+} ion (valence shell configuration: $5d^5$, $J=5/2$) should be metallic. However, this is not found to be the case. One theory to explain its electronic state proposes that the Ir^{4+} ions are present in an effective $J=1/2$ state [30]. Because of the octahedral symmetry of the crystal field surrounding Ir ions, the d-orbitals split, as described earlier, into higher energy e_g orbitals, and lower energy t_{2g} orbitals. The crystal field splitting is quite large for the 5d Ir ion compared to the electron pairing energy, and hence a low spin state is obtained where all 5 electrons occupy the t_{2g} orbitals. The strong spin-orbit coupling further acts on these levels to split them into two fully filled $J_{\text{eff}} = 3/2$ orbitals and one half-filled $J_{\text{eff}} = 1/2$ state. The band formed by this $J_{\text{eff}} = 1/2$ state is rather narrow. Even moderate correlations, like those present in Iridates, can open up a Mott gap, making the material a Mott insulator [31]. It is for this state that the realisation of unusual properties and phases have been predicted.

Summary

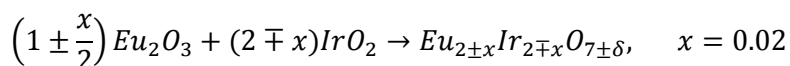
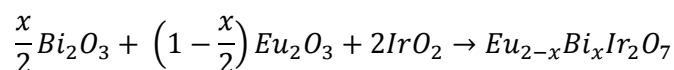
The pyrochlore Iridates are a family of compounds whose behaviour is governed by several competing factors such as their structure, crystal field effects, electronic correlations and spin-orbit coupling. The interaction of all these factors gives rise to a complex scenario out of which several unconventional phases are predicted to emerge. These phases are relevant in the context of a new understanding of quantum condensed matter as well as its applications in the fields of quantum computation and spintronics.

Experimental Techniques

2.1 Sample Synthesis

All samples used in this study were prepared using the solid state synthesis procedure. This is the simplest, most commonly used technique for the synthesis of polycrystalline solids, wherein the reactants in powdered form are thoroughly mixed and heated at high temperatures. The kinetic energy acquired by the reactant molecules due to the temperature enables them to diffuse through each other, collide in the process and form the product. In order for the reaction to happen, temperatures have to be very high, sometimes as high as 1000 – 1500°C. The surface areas of the reactants available for collision must also be large, which is why it is preferable to have finely ground samples. The contact between the grains of the reactant solids can be maximised by pressing them into pellets. [32]

Two series of samples were prepared according to the set of reactions:



The reactants used were Bi₂O₃ (Sigma Aldrich, 99.9%), Eu₂O₃ (Sigma Aldrich, 99.9%), IrO₂ (Sigma Aldrich, 99.9%).

The first series was prepared with the aim of studying the effects of Bi substitution on the Eu site, while the second one was prepared to study the effect of Eu-Ir disorder. The reactants were taken in stoichiometric quantities so as to form 1 to 1.5 g of the product and were mixed together thoroughly for 15-20 minutes using an agate mortar and pestle. They were placed for sintering in alumina crucibles in a box furnace. The sintering temperature and duration respectively were 790°C and 12 hours in the first step. Following this, the sintering temperatures were increased gradually in steps of 10 – 20 °C to temperatures of 1000-1050°C, depending on the compound as well as the weight loss in the previous sintering cycle. Grinding of the reaction mixture was done before each sintering step. Since Iridium has a melting point of 1100 °C and has a high vapour pressure in the sintering temperature range, it is necessary to increase the sintering temperature in small steps. In general, the pyrochlore phase A₂Ir₂O₇ forms with some difficulties and unless repeated grinding/sintering steps are carried out, some of the IrO₂ and A₂O₃ remains unreacted.

After 3-4 rounds of sintering, the powder samples were pressed into pellets of 13-mm diameter in a KBr Press by applying pressures of nearly 10 tons and sintered further. Towards the end of the sintering process, the samples were characterised using powder X-ray diffraction to assess the purity of the obtained product to decide on the temperature for the succeeding sintering step.

2.2 Sample Characterisation

2.2.1 X-Ray Diffraction

Powder X-Ray Diffraction is a very commonly used technique to analyse the structure of crystalline materials. It is based on the principle of constructive interference of X-rays scattered by a crystalline sample. The periodic arrays of atoms in a crystal can be visualised in the form of atomic planes. If X-ray radiation is incident on them such that its wavelength is comparable to the distance between these planes, then the crystalline structure behaves like a three-dimensional diffraction grating. The diffracted X-rays then follow the following condition for constructive interference:

$$2d\sin\theta = n\lambda$$

Where 'n' is the order of diffraction, ' λ ' is the wavelength of X-rays used, 'd' is the inter-planar spacing and θ is the angle of the incident x-ray beam with the plane of the sample.

X-rays are typically generated by accelerating high energy electrons from a cathode using a high voltage generator. A commonly used anode is a copper target. As the electrons move through the target, the repulsion by the target electrons causes them to decelerate quickly, and release energy in the X-ray region of the electromagnetic spectrum. When the source electrons have enough energy to dislodge electrons from the inner shell of the target atom, then electrons from higher orbitals fill the empty shells, emitting a spectrum characteristic to the target atom in the process. The most intense components of the characteristic spectrum are the K_{α} and K_{β} components, which represent a transition of electrons of the second (L) shell and third (M) shell respectively, to the innermost (K) shell. The emitted spectrum is filtered by monochromators to give a single wavelength which can be used for powder X-ray diffraction. For the Cu target, this radiation has a wavelength of 1.5405 Å.

The X-ray beam is focussed onto the sample. The angle of incidence is varied continuously to obtain the intensity as a function of the angle, which is recorded electronically. Whenever the incident X-rays satisfies the Bragg Law for constructive interference, the intensity peaks. Each intensity peak corresponds to a Bragg plane. Since crystals with different symmetries have different characteristic Bragg planes, this method can be used to differentiate between crystal

structures, and also to characterise crystals with unknown structures. The angular positions of a peak can also be correlated to the inter-planar spacing of the corresponding Bragg plane. This information can be used to obtain the lattice parameter of the unit cell of the crystal being observed.

In order for the X-rays to 'access' all the crystal planes, the sample must be aligned in the direction of each of the planes. A simpler way to obtain reflected x-ray for each set of planes is to use a powdered form of the crystal such that there are many crystalline planes oriented in all possible directions, and each one is available for diffraction. To attain this condition, the sample must be finely ground so that there is no preferred orientation in the crystal.

Powder X-ray Diffraction for this study was carried out using a Bruker D8 Advance Powder X-Ray Diffractometer in the θ - θ geometry. The prepared samples were ground into a fine powder and then mounted on a glass slide using a thin layer of oil as an adhesive. This sample thus prepared was placed in the diffractometer. The glass slide as well as the oil are amorphous and hence don't contribute to the XRD spectrum.

The patterns obtained were compared to the standard patterns recorded in a database from the International Centre for Diffraction Data (ICDD).

To complement the structural data obtained by X-Ray diffraction about the phases present in the compound, information about the composition can be obtained through Scanning Electron Microscopy and Energy Dispersive X-ray Spectroscopy.

2.2.2 Scanning Electron Microscopy and Energy Dispersive X-Ray Spectroscopy

Scanning electron microscopy (SEM) and Energy Dispersive X-Ray Spectroscopy (EDS) are used to study the morphology and composition of a sample, respectively. For both measurements, a focused beam of electrons is positioned on the sample of interest; the electrons from the beam interact with the sample in various ways, leading to emission of a variety of electrons and/or photons. These emissions are then detected via a detector to generate an image or a composition map of the sample.

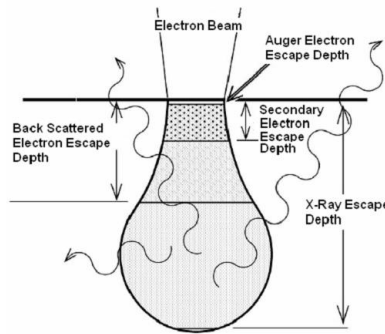


Fig 2.1 Signals emerging from electron beam-sample interaction [33]

The signals used to characterise the samples are briefly described below:

An electron beam passing near an atom in the sample may impart some energy to the electrons in a sample, thereby ionising it. Electrons ejected thus are called *secondary electrons*. Since they have relatively low energies, only secondary electrons generated near the surface of the sample can reach the detector. Thus these electrons give information about the topology of the sample.

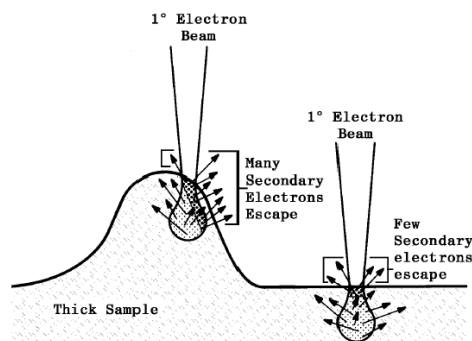


Fig 2.2 Contrast in the secondary electron signal due to surface topology [33]

Another kind of signal is obtained when electrons of the sample atoms occupy the levels which were left empty by the secondary electrons. These transitions are accompanied by the emission of X-ray photons whose energy is equal to the difference in the energies of the two levels. Since the energy levels of the electrons are characteristic of the atoms, the wavelengths of the emitted X-ray photons are characteristic wavelengths as well. This spectrum of X-rays gives an indication of the chemical composition of the sample. Since X-rays have high energies, and are not charged, they don't face any hindrance from the sample atoms so even signals from deep inside the sample can be detected.

The electron beam has to be accelerated by an excitation voltage and focused using electrostatic lenses. The excitation voltage of the electron beam depends on the kind of signal

that we want to receive. For imaging the surface, i.e. to obtain secondary or back-scattered electrons, lower voltages are better; surface details can be enhanced better if the electron energies are low enough for the beam to be restricted to the surface.

EDS is typically carried out at 15-20 keV, but the most optimum value of the excitation voltage depends on the atoms present in the sample. While higher excitation voltages might seem to imply better penetration and hence more data from the interior of the sample, a caveat that must be kept in mind is that if incident electrons penetrate to a very large extent, the emergent beam is more likely to be absorbed before reaching the detector. Thus the intensity received is lesser and may introduce errors while doing quantitative analysis. The spatial resolution can also be affected by using an excessive over voltage. An empirical rule to select the excitation voltage (in kV) is that it should be at least twice the energy (in keV) for the highest excitation line to get sufficient intensity, and at most 10-20 times the energy of the line of interest of the lowest energy.

Another thing to be kept in mind while performing EDS on a sample is that the EDS detectors are not very accurate in the detection of elements with lighter nuclei, such as oxygen. While obtaining compositional information about the elements in a material, only the relative ratios of heavier atoms can be considered as reliable, since the poor detection of oxygen leads to incorrect estimation of absolute values.

Scanning electron micrographs and energy dispersive X-ray spectra were taken for the synthesised samples using a Zeiss Ultra Plus Scanning Electron Microscope. The accuracy of composition determination is around 1-2%. Flat sections from the sintered pellets were dry cut using a low-speed saw and placed on double sided carbon tape, which was then mounted onto SEM stubs. For each sample, multiple points and areas on the surface were selected randomly and surface morphology and elemental composition were recorded. EDS spectra were taken at 20, 25 and 27 kV and the results were compared.

2.3 Measurement of Physical Properties

The magnetic and transport properties of the prepared samples were studied. Most of these measurements were performed using the Physical Property Measurement System Evercool-II by Quantum Design. Resistivity measurements down to 80 K were also performed on a few samples using a home-built set-up.

2.3.1 The Physical Property Measurement System

The Physical Property Measurement System is an apparatus that can measure a variety of magnetic, electric and thermal properties in the temperature range of 2 – 400 K and in

magnetic fields of up to ± 9 Tesla. The PPMS consists of a super-insulated Dewar that encloses a sample chamber which is surrounded by liquid Helium. Various measurement probes are also provided onto which samples can be loaded and lowered into the sample chamber. In this chamber, which is sealed from the external environment, temperatures and magnetic fields can be varied according to the experimental requirements.

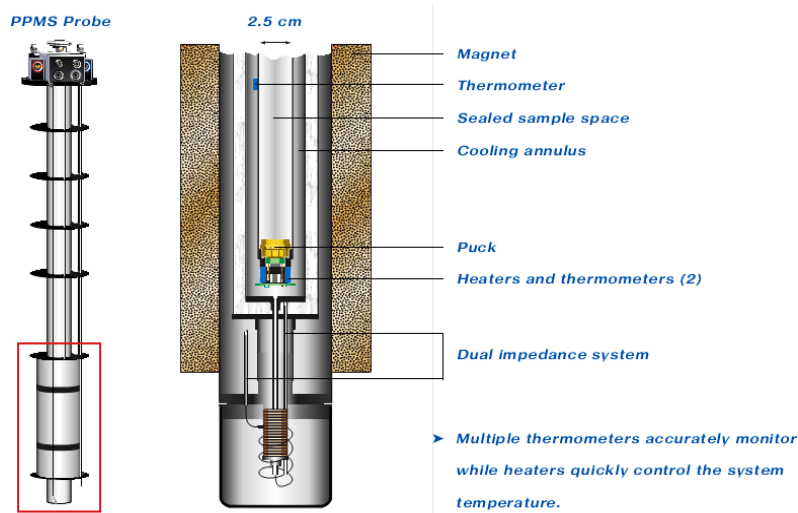


Fig 2.3 The sample chamber of the PPMS [34]

The temperature of the sample chamber is controlled by the means of a heater present at the base of the sample chamber and by flowing helium vapour in the cooling annulus (as shown in the figure 2.3). The magnetic fields are controlled using a superconducting coil immersed in liquid Helium, which can generate fields up to 9 Tesla. All user commands such as sequence of measurement, rate of temperature variation and so on are relayed to the instrument by an interface called PPMS MultiVu.

2.3.2 Transport Property Measurements

Electrical resistivity was measured as a function of temperature for the prepared samples. For measurements in the PPMS as well as in the home-built setup, the four probe method of resistivity was employed. In the home-built resistivity set-up, KEITHLEY model no.6221 (current source) and 2182A (Nanovoltmeter) were used. The temperature was measured using a platinum resistance thermometer.

Four Probe Method: The four probe method is a technique used for accurate measurements of a sample's resistivity.

Typically, for electrical transport measurements an electric current is passed through the samples and the voltage drop across them is measured. This gives the value of the sample resistance. The resistance of the sample is dependent on the geometry of the sample,

whereas the resistivity is a characteristic property of a material. The resistivity of a sample, ρ , can be obtained from the measured values of resistance by the following equation:

$$\rho = R \frac{A}{l} = \frac{V \cdot A}{I \cdot l}$$

Where R is the resistance, A is the cross-sectional area perpendicular to the direction of current flow and l is the length across which the voltage drop is measured i.e. the distance between the two voltage-sensing terminals; I is the current passed through the sample and V is the measured voltage drop across the terminals.

One way of doing this, known as the two-probe method, is passing a known constant current across the sample and measuring the voltage drop created across the terminals which are passing the current. The main disadvantage of this method is that the measured resistance has a contribution from the contact resistance of the measuring leads as well. To eliminate this, the voltage and current terminals can be separated so that there are four terminals on the sample. The voltage terminals are placed in between the current terminals so as to exclude the voltage drop due to the contact resistance of the current terminals. Since a voltmeter has a very high resistance (typically in the order of M Ω) and negligible current passes through it, the voltage drop due to the contact resistance of the voltage terminals is also low. This leads to measurement of a more accurate value of resistivity.

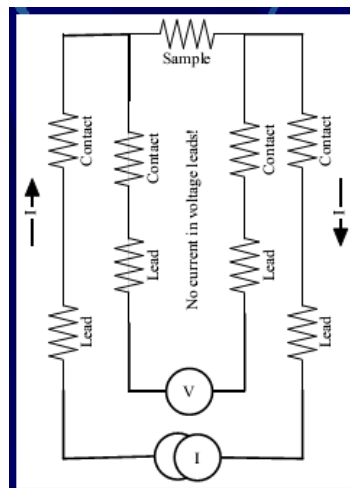


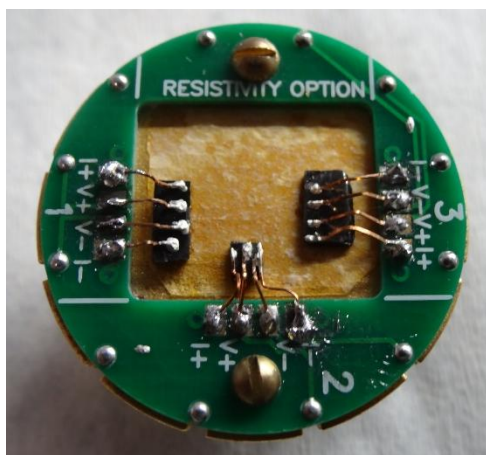
Fig 2.4 Four Probe Method for Resistivity Measurement (Source: Documentation for PPMS AC Transport Option, Materials Research Laboratory, UCSB)

Resistivity measurements were performed in the PPMS between 2-300K, while those on the home built setup were performed from 77K (boiling temperature of liquid nitrogen) to 300K. While temperature control in the PPMS can be dictated through the PPMS MultiVu software,

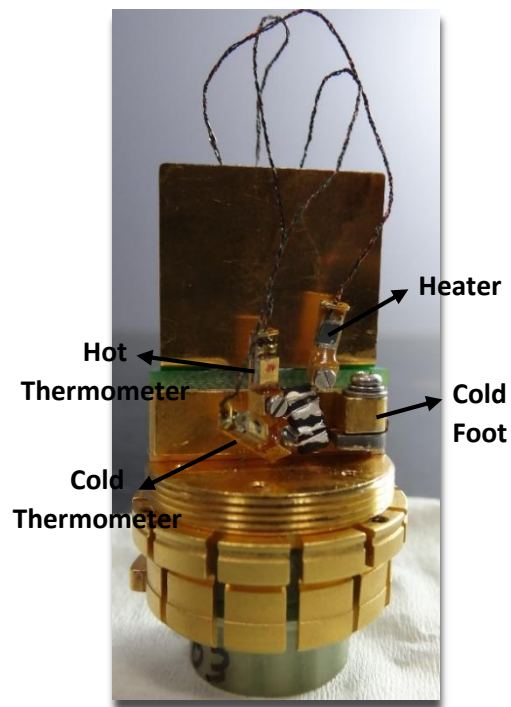
in the home built set-up, the sample is lowered down and raised up a liquid nitrogen Dewar in a controlled manner using a stepper motor assembly.

The sample was attached to the sample holder via GE Varnish, which is thermally conducting but electrically insulating and thus prevents shorting of the sample with the base plate of the holder. A layer of thin cigarette paper was also glued using GE varnish in between the sample and the base in order to further lower the chances of electrical shorting. Contacts were made by placing one end of each of four copper wires, which were soldered onto the sample holder on their other end, on the sample surface and connecting it to the sample using PELCO® Colloidal Silver paste. The contacts were allowed to cure overnight at room temperature or for 1 - 2 hours in a dry box (~ 60 °C) before starting the measurement.

Resistivity was also measured for a few samples using two different probes provided with the PPMS apart from the DC resistivity probe. These were the Thermal Transport Option and the AC Transport option. The AC Transport sample holder is similar to that of the DC resistivity holder. The Thermal Transport Measurement setup can be used to measure thermal conductivity, thermopower and electrical resistivity. Four copper wire-contacts are attached to the rectangular sample using silver paste and then three of them are screwed into gold-coated shoes which serve as thermometers and a heater, while one goes into the heat sink. Samples mounted onto the dc resistivity sample holder and the thermal transport option sample holder are shown in the following figure:



a.



b.

Fig 2.5 Sample pellets mounted onto sample holders of a. DC Resistivity setup and b. Thermal Transport Option

Since the samples were conducting, excitation currents of around 5 mA were used. The dimensions of the samples (area of cross-section and length between voltage probes) were measured before loading them on the instruments to obtain resistivity from the measured resistance values.

Among the main sources of error is incorrect measurement of sample dimensions. A sample is likely to have a non-uniform cross-sectional area unless cut very carefully. This possibility can be taken care of by using a crystal-cutting low speed saw to cut samples in a regular cuboidal shape. Internal micro-cracks in the samples can also give rise to step-like features in the resistivity besides augmenting the uncertainty of the measured value. Another source of error is the measurement of the distance between the voltage probes. This is because the electrical contacts made with the silver paint are not point contacts, but are spread out over a finite area. This error can be minimised by taking an average over the distance between the outer ends of the two silver spots and the inner ones. Despite all such precautions, the typical error in these measurements can be estimated as at least 20% of the measured value.

2.3.3 Magnetic Property Measurements

Magnetisation is measured as a function of temperature under a fixed applied field, and as a function of applied magnetic field for a given temperature. Most of the measurements were carried out using a Vibrating Sample Magnetometer (VSM) probe associated with the PPMS. The principle of operation is based on Faraday's Law of Induction, which states that when the magnetic flux inside a conducting circuit changes, an emf is produced which is proportional to the time rate of change of the flux.

If a sample with a non-zero magnetic moment is vibrated inside a coil of conducting wire, then for a fixed frequency, the voltage induced in the coil will be proportional to the magnitude of the sample's magnetic moment. The PPMS VSM uses this principle for the magnetisation measurements. To nullify the signal that may arise due to the changing external magnetic field, a highly sensitive gradiometer pickup coil is used. The sample is located at the vertical centre of this coil and is oscillated sinusoidally at a frequency of 40 Hz. The amplitude of oscillation can be varied from 1-3 mm. The emf induced in the pickup coils is amplified and then measured using the lock-in technique. The measured voltage is calibrated in the electromagnetic (emu) units.

M vs. T measurements: These measurements seek to study how the magnetisation of a sample varies with temperature at a constant magnetic field.

The measurement sequence typically involves cooling the sample from room temperature down to $T = 2$ K under zero applied field initially (zero-field cooling or ZFC), measuring the magnetisation at a constant field while warming up to room temperature, cooling it again down to 2 K, under the same applied field (Field Cooling or FC), and then measuring the moment under the same field up to room temperature. Transitions to ordered phases show up in the form of anomalies in the magnetisation versus temperature plot. For example, simple Neel type antiferromagnetic ordering manifests itself in the form of a cusp; at a ferromagnetic ordering transition, the magnetisation shows a step like increase. On the other hand, a spin-glass transition typically shows a cusp in the ZFC magnetisation but under the FC scan the magnetisation either remains constant or increases gradually below the cusp temperature giving rise to significant thermomagnetic irreversibility. In general, ZFC-FC splitting may arise for many other reasons; for instance superparamagnets exhibit this property when cooled below their so-called blocking temperature. In some ferromagnets the splitting may appear due to domain wall motion.

M vs. H measurements: These measurements are done keeping the temperature constant and varying the magnetic field. These measurements can indicate whether a material is paramagnetic (in which case a plot of moment M versus field H shows a Brillouin function dependence discussed in the first chapter of this thesis) or orders magnetically. Ferromagnets below their characteristic Curie-temperature are easier to identify as they show hysteresis behavior when measured over all four quadrants. Antiferromagnets in their ordered state exhibit a linear $M(H)$. In some exceptional cases, field induced transitions (spin-flip or spin-flop) can also be observed under moderate applied magnetic fields.

The VSM attachment provides two ways of mounting samples – one of these is for powder samples. A non-magnetic capsule is filled with the required amount of sample and placed in a brass holder. This is attached to a sample rod which lowers the sample down to the centre of the pickup coils. The other method is used for mounting small flat sections cut from polycrystalline pellets or single crystals. In this method, the sample is glued using GE varnish to a quartz sample holder and secured with non-magnetic Kapton tape. For samples with intrinsically weaker magnetic moment the quartz mounting option is preferred as it provides a smaller background signal.

Our measurements were performed on pellets. Pellets were preferred over powder because they are compact and do not allow oxygen to be trapped within the samples – thus for samples

with low moment, the problem of a weak spurious anomaly associated with the paramagnetic to antiferromagnetic transition of oxygen at 43 K can be eliminated to a great extent.[35]



Fig 2.6 One of the sample pellets glued to the quartz sample holder for VSM measurements

M-T measurements were performed in ZFC and FC mode on all the samples under a field of 1 kOe, while M-H measurements were performed between -80 kOe to + 80 kOe. The temperatures were selected according to the behavior of the samples. Thus, while for most samples, M-H measurements were done at 2K and 300K; for $\text{Eu}_2\text{Ir}_2\text{O}_7$, the measurements were taken at 2, 10, 122, 125 and 300K.

To obtain information on whether the compound shows spin-glass behaviour, AC susceptibility was measured over a small temperature range around the transition temperature at several frequencies of the AC field.

2.3.4 Heat Capacity

In the PPMS, heat capacity is measured by controlling the heat provided to the sample and measuring the corresponding change in temperature. The sample is mounted on a platform using a thin layer of Apiezon N grease, which keeps it in a good thermal contact with the platform. The heater and thermometer are integrated directly on the sample platform.

At the beginning of each experiment, addenda measurement is done with a layer of freshly put Apiezon N grease on the sample platform. This is the measurement of the heat capacity of the sample holder and the grease. The sample (typically 3-4 mm x 3-4 mm in cross-section and 1 mm thickness) is then mounted with the same grease (no grease is added or removed during sample mounting) and measured. The sample heat capacity is obtained by subtracting the addenda heat capacity from the total measured heat capacity. High vacuum is prerequisite for these measurements so that unaccounted heat losses via conduction can be minimised. In this thesis, specific heat was measured from 2-200K for $\text{Eu}_2\text{Ir}_2\text{O}_7$. Specific heat measurements were also done in the presence of a magnetic field.

Results and Discussion

3.1 Structural Characterisation

The samples prepared during the course of this work were thoroughly characterised using powder x-ray diffraction and Scanning electron microscopy. We first present our results of the powder x-ray diffraction. Fig 3.1 shows the XRD Data of $\text{Eu}_2\text{Ir}_2\text{O}_7$ analysed using the Rietveld Refinement method, which confirms the formation of the compound in a single pyrochlore phase (cubic with $\text{Fd}3\text{m}$ symmetry).

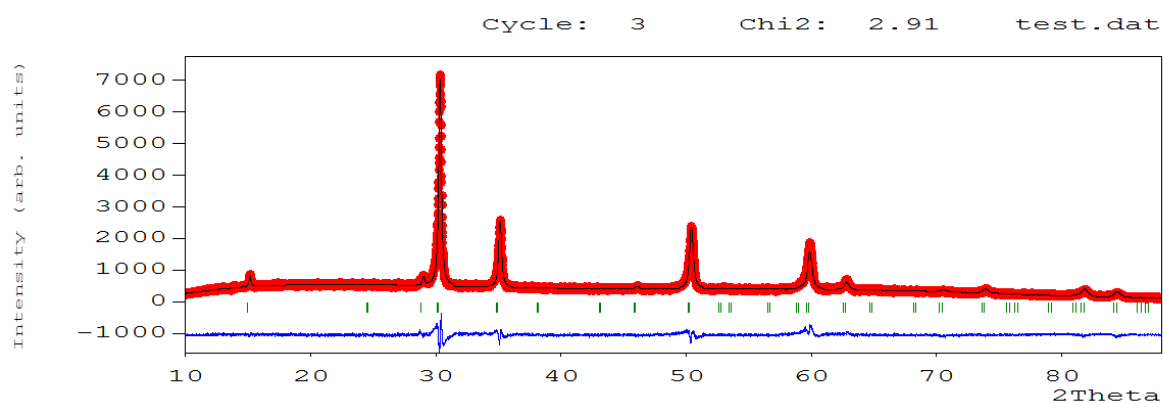


Fig 3.1 The Rietveld refined XRD pattern for $\text{Eu}_2\text{Ir}_2\text{O}_7$

Fig. 3.2 shows the powder x-ray diffraction (PXRD) pattern of the samples $\text{Eu}_2\text{Ir}_2\text{O}_7$, $\text{Eu}_{2.02}\text{Ir}_{1.98}\text{O}_7$ and $\text{Eu}_{1.98}\text{Ir}_{2.02}\text{O}_7$. All three samples crystallise with the pyrochlore structure. In particular, all the diffraction peaks could be indexed based on the $\text{Fd}3\text{m}$ space group indicating that secondary phases, if present, are beyond the detection limit of the PXRD technique. In the inset of Fig. 3.2, an exaggerated view of the data is shown in the neighborhood of the peak 440. This is done to emphasise that 2 % Eu-Ir off-stoichiometry neither changes the position nor the line shape of the diffraction peaks, which also means that the lattice parameter 'a' shows no measurable change within the resolution limit of our PXRD.

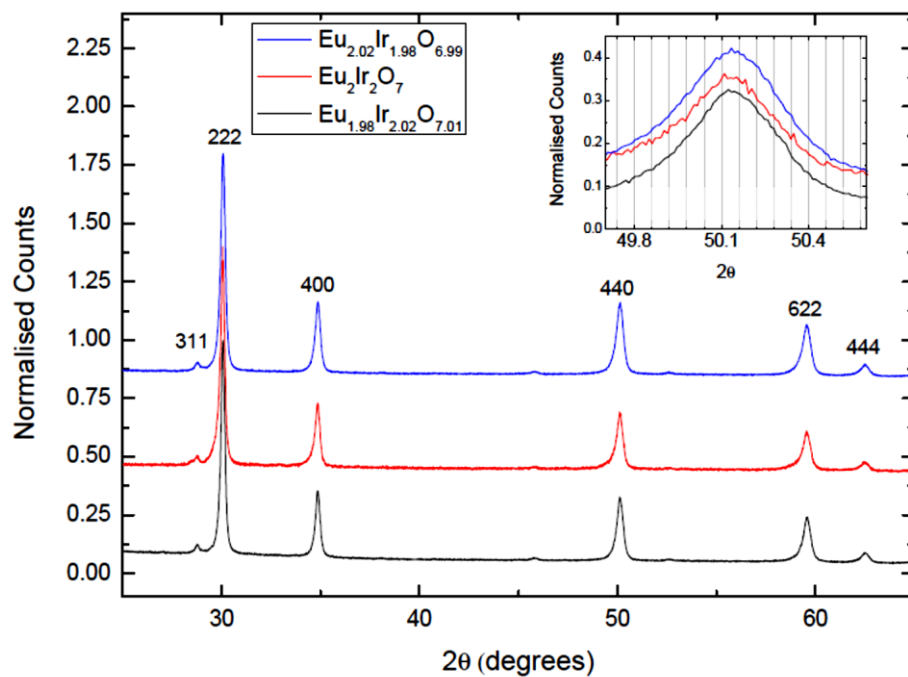
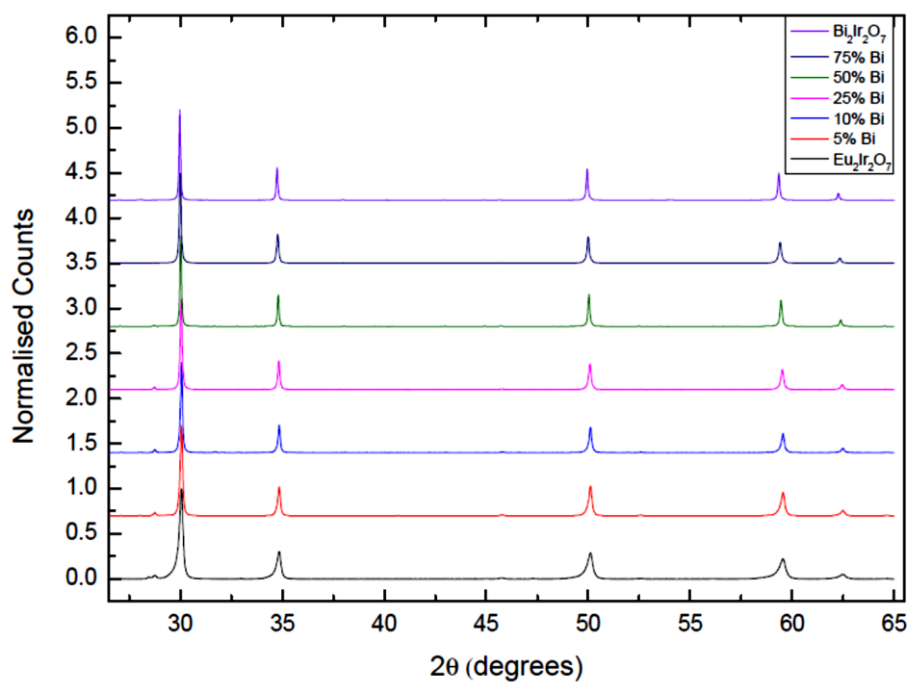


Fig 3.2 Normalised XRD Spectra of $\text{Eu}_{2\pm x}\text{Ir}_{2\mp x}\text{O}_{7\pm\delta}$ ($x = 0, 0.02$). Inset: an exaggerated view of the 440 diffraction peak for the three compositions (vertical grid is guide to the eye)



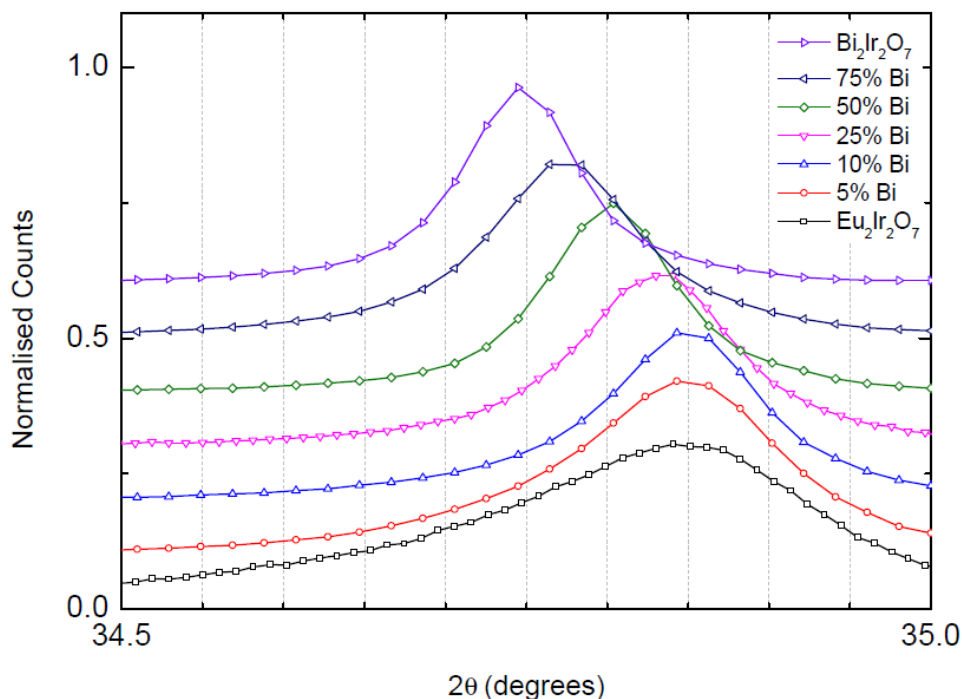


Fig 3.3 (a) Normalised XRD Spectra of the Bi-Eu series of compounds, **(b)** The 622 peak position in the XRD spectrum as a function of Bi composition.

Fig. 3.3 a shows the PXRD of the series of samples $\text{Eu}_{2-x}\text{Bi}_x\text{Ir}_2\text{O}_7$ for $x = 0, 0.1, 0.2, 0.5, 1, 1.5$ and $\text{Bi}_2\text{Ir}_2\text{O}_7$. The PXRDs show the formation of the pyrochlore phase. It was found that the synthesis required multiple sintering/grinding cycles to get the desired phase without impurities. In particular, we observed that the closer the composition was to $\text{Bi}_2\text{Ir}_2\text{O}_7$, the easier it became to obtain the compound in a single-phase. While $\text{Bi}_2\text{Ir}_2\text{O}_7$ formed at a temperature of $875\text{ }^\circ\text{C}$, the other samples all required temperatures of above $1000\text{ }^\circ\text{C}$ to form. Minor diffraction peaks corresponding to some unreacted IrO_2 were also observed for some of the samples. These are not discernible in the Fig. 3.3 because their relative intensities are very small. From the ratio of the intensities we estimate the quantity of unreacted IrO_2 to be around 1 % or less, which is further corroborated by the SEM studies reported in the next section.

In Fig, 3.3b, an exaggerated view of the 622 diffraction peak is shown to emphasise the variation of the lattice parameter and the diffraction line shape upon gradual replacement of Eu by Bi. Since the ionic radius of Bi^{3+} is larger than that of Eu^{3+} , we expect the lattice parameter to increase with increasing x . The lattice parameters were calculated using the software UnitCell [36]. Fig. 3.4 shows the obtained lattice parameters plotted against the percentage of Bismuth. The numerical values of the lattice parameters for various x values are presented in table 3.1.

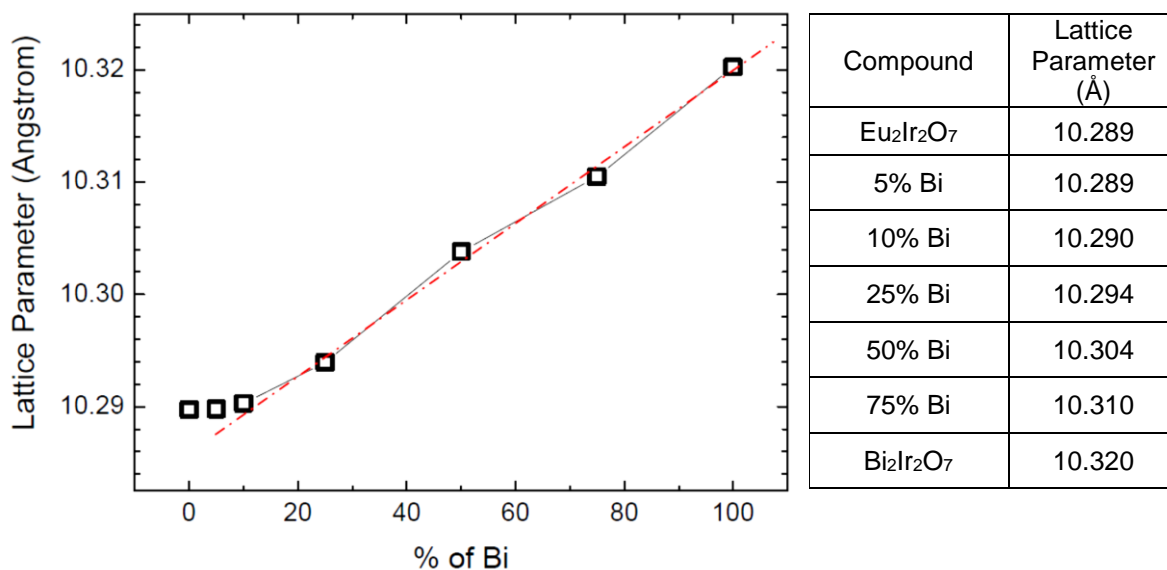


Fig 3.4 Variation of lattice parameter as a function of percentage of Bismuth in the composition. The error bar is roughly the size of the data point (i.e., 0.002 Å). The red line is a guide to the eye.

Table 3.1 Lattice parameters of all the synthesised samples

The lattice parameters show a linear decrease as expected on going from Bi₂Ir₂O₇ to Eu₂Ir₂O₇. However, close to the Eu end, the lattice parameters do not show an appreciable change for 10 and 5 % Bi-doped samples. A similar behavior has previously been observed for the analogous series Y_{2-x}Bi_xIr₂O₇ [37]. In another analogous solid solution series between the end member pyrochlores Gd₂Zr₂O₇ and Nd₂Zr₂O₇, however, the lattice parameter shows the expected linear variation [38].

The ambiguity observed in our study may not appear as striking if one notes that the lattice parameter of Bi₂Ir₂O₇ (10.327 Å) is smaller than that of Pr₂Ir₂O₇ (10.406 Å) despite the fact that the ionic radius of Bi³⁺ (1.170 Å) is greater than that of Pr³⁺ (1.126 Å).

Bi₂Ir₂O₇ doesn't follow the linear variation of the lattice parameter with ionic radius of the rare-earth iridate series (see Fig. 3.5). To verify this observation in the series synthesised here, the average A-site ionic radii were plotted against the experimentally obtained lattice parameters. They were found to follow a linear relationship (shown using red circles), but it did not fit in with the one followed by the rare-earth series as shown in Fig. 3.5 (shown using black squares).

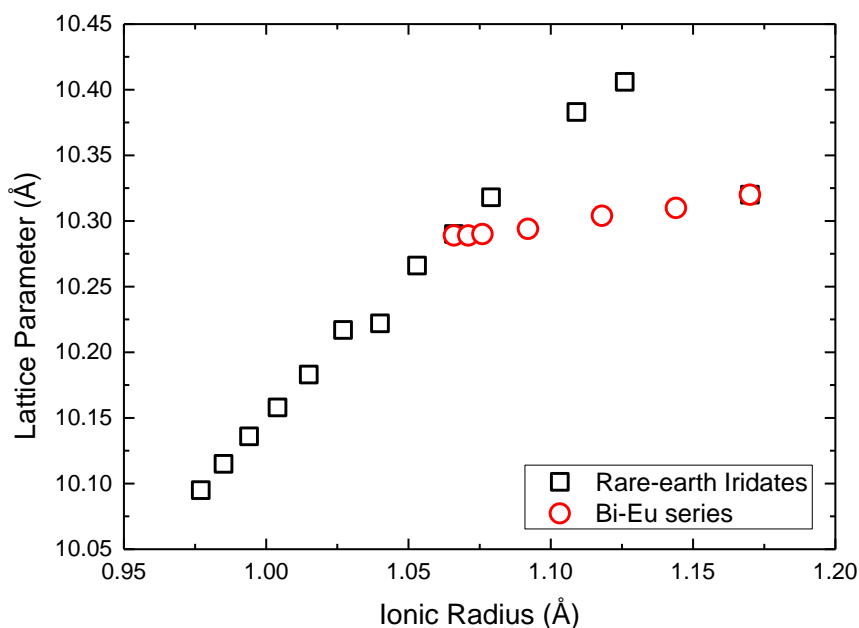


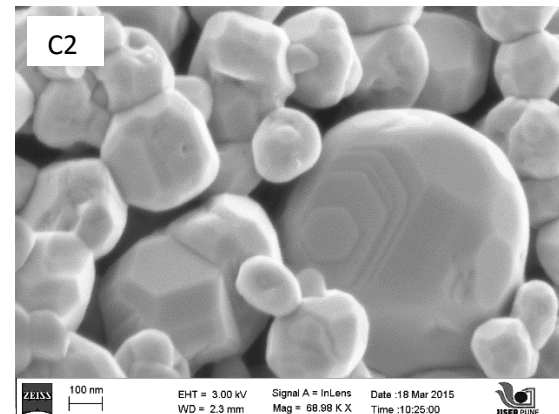
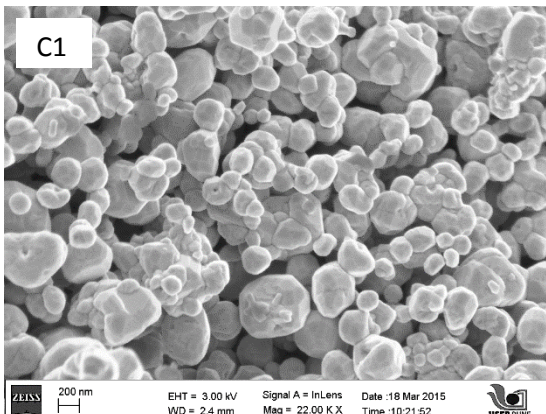
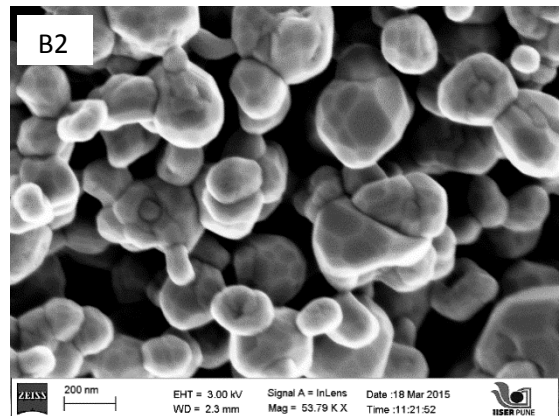
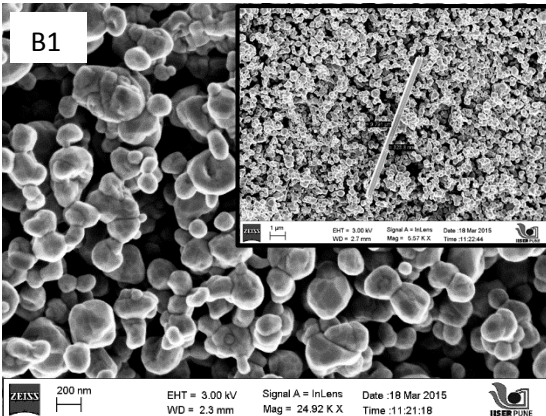
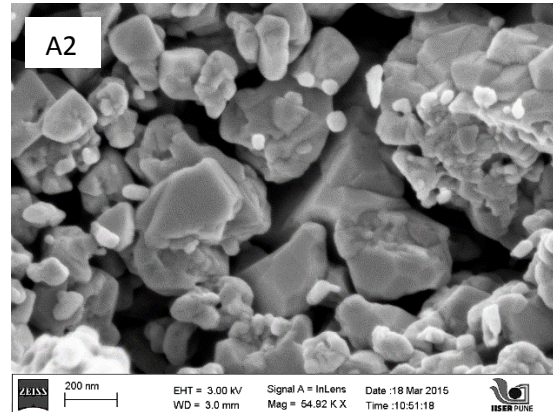
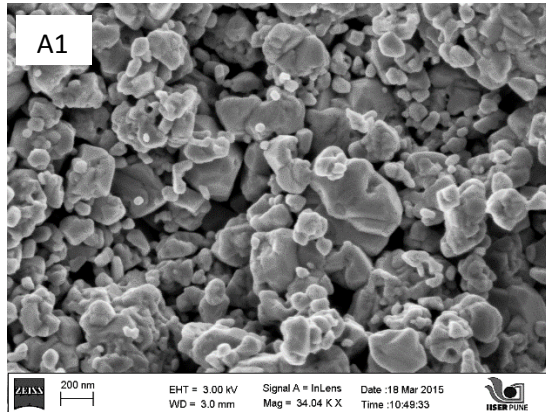
Fig 3.5 Ionic radii plotted versus lattice parameters for the rare earth series and the Bi-Eu series [7]

The lattice parameter obtained in each intermediate composition (and $\text{Bi}_2\text{Ir}_2\text{O}_7$) was lower than what would be expected for a rare-earth ion corresponding to the same ionic radius. This seems to imply that Bi^{3+} in the pyrochlore iridates does not behave like trivalent rare-earth ions. This is also supported by ref. [39] where it is noted that the lattice parameters of the metallic pyrochlores $\text{Bi}_2\text{M}_2\text{O}_7$ (where $\text{M} = \text{Ru}, \text{Rh}$ and Ir) are smaller than the values expected by extrapolating from the corresponding rare-earth pyrochlores of Ru, Rh and Ir. On the other hand, the lattice parameter of the insulating pyrochlores $\text{Bi}_2\text{Sn}_2\text{O}_7$ fall in line with that of the corresponding rare-earth pyrochlores (see, for example, Fig. 2 in ref. [39]). It has been proposed that this observed anomalous lattice parameter variation of the metallic Bi pyrochlores could arise as a result of mixing between Bi 6s and the 4/5d orbitals of the transition metals leading to a reduction of the lone pair character of the Bi 6s electrons.

It should be observed that the peak shape for $\text{Eu}_2\text{Ir}_2\text{O}_7$ appears to be broadened and asymmetric as compared to that of the other compounds in the Bi-Eu series. Upon moving towards $\text{Bi}_2\text{Ir}_2\text{O}_7$, the peaks gets sharper and more symmetric. This could be due to the microstructure of the samples, as will be discussed in the next section.

3.2 Microstructure and Composition

Some representative SEM images obtained for all the synthesised samples in the Bi-Eu series are shown in Figure 3.5.



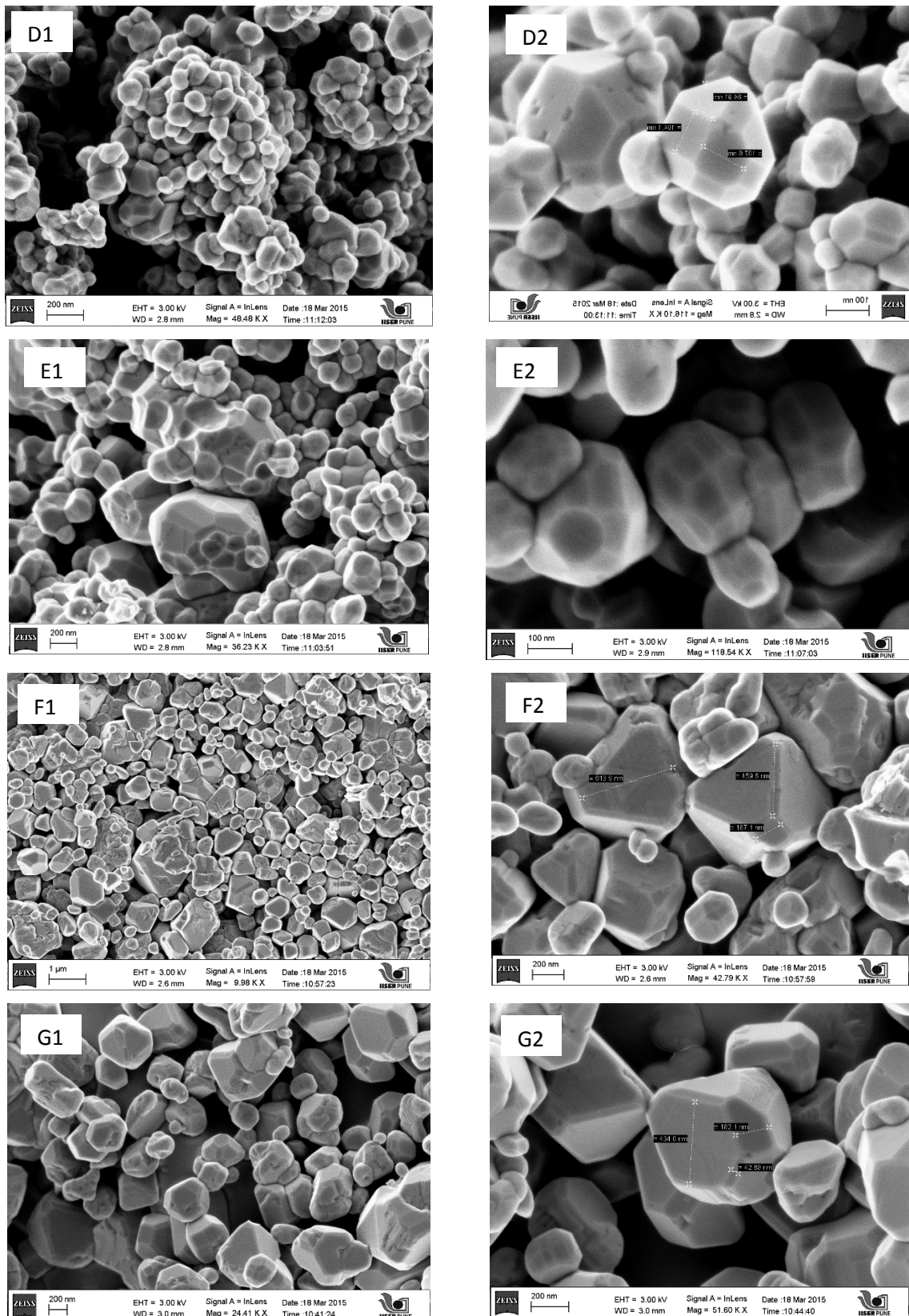


Fig 3.6 The figures A-G represent SEM images of the synthesised samples. A1, A2: $\text{Eu}_2\text{Ir}_2\text{O}_7$; B1, B2: 5% Bi; C1, C2: 10% Bi; D1, D2: 25% Bi; E1, E2: 50% Bi; F1, F2: 75% Bi; and G1, G2: $\text{Bi}_2\text{Ir}_2\text{O}_7$, respectively. The inset in Fig. B1 shows the presence of IrO_2 rods in the 5% Bi composition

From the SEM images in Fig. 3.6, it can be seen that the grain size shows a large variation in any given sample. However, upon moving from $\text{Eu}_2\text{Ir}_2\text{O}_7$ towards $\text{Bi}_2\text{Ir}_2\text{O}_7$, the structure of these grains seems to become more well-defined. In particular, in the 75% Bi sample and in the sample $\text{Bi}_2\text{Ir}_2\text{O}_7$, the grains have a truncated octahedral shape similar to that shown by single crystals grown using the high temperature flux growth method [40]. The dimensions of some of these single crystalline grains were found to be as large as roughly 500 nanometers for the triangular faces of the octahedra. This trend of obtaining well-formed crystals for higher Bi-concentrations probably reflects the ease of compound formation with increasing Bi content. One possible explanation could be that since the reactant Bi_2O_3 has a low melting point ($\sim 820^\circ\text{C}$) its mobility could be very high at temperatures close to the melting point, leading to better diffusion through the reaction mixture during the sintering process carried out close to this temperature.

This trend could probably be correlated to the observations we made on the data obtained using XRD. Since the polycrystals closer in composition to $\text{Bi}_2\text{Ir}_2\text{O}_7$ have a more well-defined microstructure, it could be the reason behind them exhibiting relatively sharper and well-defined diffraction peaks. The lack of a well-defined microstructure in $\text{Eu}_2\text{Ir}_2\text{O}_7$ polycrystals could be the reason behind its asymmetric peaks.

All the samples seem to have formed uniformly, as can be seen from the lack of any phase contrast and the absence of morphologically different grains in the images that would suggest a secondary phase. However, the composition containing 5% Bi showed rod-like structures in some of its SEM images, as shown in the inset of Fig. 3.6 b. Using EDS, the composition of these rods was found to be that of IrO_2 , which couldn't be very clearly detected in the powder XRD data. In the other samples, no such rod-shaped microcrystals were detected in the areas scanned.

To find out if the samples were formed in the correct stoichiometry, and to detect any impurity phases that could be present, Energy Dispersive X-Ray Spectroscopy (EDS) data was recorded. EDS spectra give information about the atomic percentages of the elements present in an area or point, based on the intensity of characteristic X-Rays received from it. The absolute values of these percentages are not reliable, because they are calculated including the signal from lighter elements like oxygen, which are very low in energy to be detected accurately. However, the relative ratio of the heavier elements can be taken to judge the stoichiometry of these elements in the sample. From the obtained atomic percentages, the ratio of Bi : Eu and that of (Bi+Eu) : Ir (i.e. A site : B site) were calculated for multiple scanning sites and then averaged over.

Before we furnish the results of our EDS experiments, it is worth mentioning here that the experimental value of the Bi : Eu ratio can be inaccurate if the experiments are not performed under the optimal operating voltage. To illustrate this point, we consider the case of the $\text{Eu}_2\text{Ir}_2\text{O}_7$ sample, which was probed using three different excitation voltages: 20 kV, 25 kV and 27 kV. The values of atomic percentages of the constituent atoms differed considerably for the three voltages. The ratios obtained for Eu : Ir are summarised in the table 3.2:

Expected Eu : Ir Ratio	20 kV	25 kV	27 kV
1	1.011	1.712	1.748

Table 3.2 Relative atomic percentages of Eu:Ir obtained using different EDS excitation voltages

The Eu : Ir ratios obtained for excitation voltages of 25 and 27 kV were nearly 2:1. Considering the argument discussed in Chapter 2 regarding how excessive voltages can lead to over-penetration and absorption of the X-Ray signal, the empirical rules discussed there can be used to obtain the optimal excitation voltage. Out of the elements present, the highest energy line, which is the Ir L α line –has an energy of 9.174 eV and the lowest energy line is the Ir M α line corresponding to an energy of 1.978 eV [41]. Thus, the most reliable values should be given by the 20 kV excitation voltage, which is actually the case for our data.

Thus 20 kV was used as the excitation voltage to analyse the rest of the samples. The obtained values are summarised in the table 3.3 given below.

Compound	Bi:Eu		(Bi+Eu):Ir	
	Expected	Observed	Expected	Observed
$\text{Eu}_2\text{Ir}_2\text{O}_7$	-	-	1	1.151
$\text{Bi}_{0.1}\text{Eu}_{1.9}\text{Ir}_2\text{O}_7$	0.05	0.057	1	0.962
$\text{Bi}_{0.2}\text{Eu}_{1.8}\text{Ir}_2\text{O}_7$	0.11	0.130	1	0.904
$\text{Bi}_{0.5}\text{Eu}_{1.5}\text{Ir}_2\text{O}_7$	0.33	0.257	1	1.051
$\text{BiEuIr}_2\text{O}_7$	1	0.856	1	1.062
$\text{Bi}_{1.5}\text{Eu}_{0.5}\text{Ir}_2\text{O}_7$	3	2.965	1	1.015
$\text{Bi}_2\text{Ir}_2\text{O}_7$	-	-	1	0.922

Table 3.2 Relative atomic percentages obtained using EDS

Considering the 1-2% instrumental error, the ratios obtained for all the samples are in good agreement with the values expected. This analysis confirms that the samples synthesised by us are stoichiometric without the presence of any parasitic phase.

3.3 Magnetic Measurements

The magnetic susceptibility as a function of temperature for all members of the Bi-Eu series is plotted in Figure 3.7. The dotted line represents the van Vleck contribution of Eu^{3+} for a λ value of 400 K.

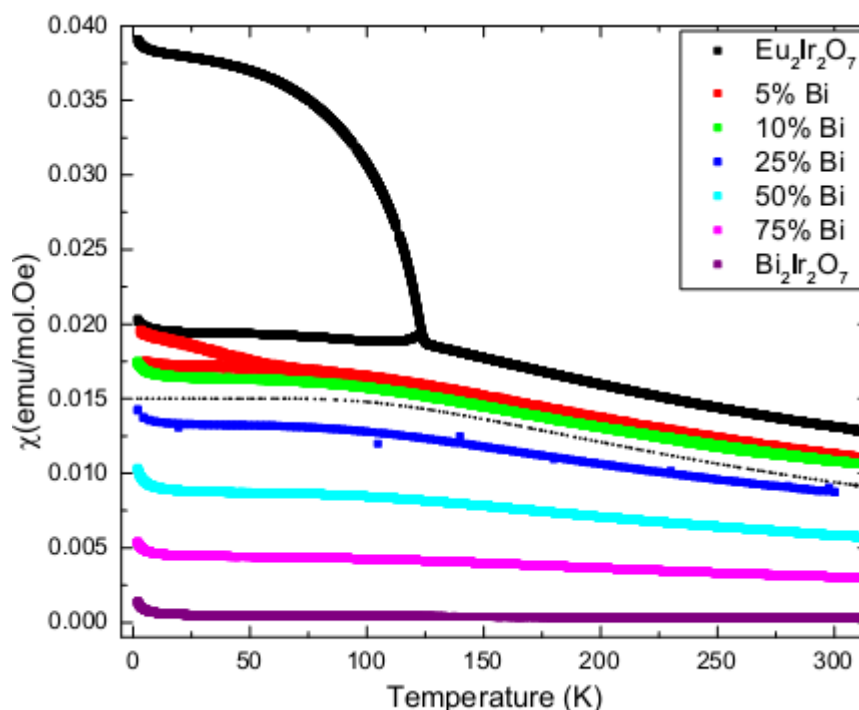


Fig 3.7 The magnetic susceptibility of the series plotted as a function of temperature

The $\text{Eu}_2\text{Ir}_2\text{O}_7$ sample shows the highest magnetic susceptibility of all the compounds in the series. For this sample, at 120 K, there is a separation between the zero-field cooled (ZFC) and the field cooled (FC) susceptibility. The ZFC curve shows a peak at 120 K, suggestive of an antiferromagnetic transition, whereas the FC curve shows a ferromagnet-like rise below this temperature, though the susceptibility is much lower than a typical ferromagnet. The ZFC-FC splitting below 120 K as well as the values of the susceptibility of our sample are comparable to those reported in the references [8] and [42] for the polycrystalline samples.

Such a splitting was initially interpreted as a spin-glass like freezing of the Ir moments. However, zero field μSR experiments done in the study [11] confirm the long-range ordering of the Ir moments below the ZFC-FC splitting temperature. This weakens the case for a spin-glass-like ground state. From the muon precession frequency (14 MHz), the size of the ordered Ir^{4+} moment is estimated to be around $0.3 \mu_B$. Therefore, the origin of the observed thermomagnetic irreversibility even for a uniformly ordered state is not well understood. However, a recent study [43] of an analogous pyrochlore iridate, $\text{Y}_2\text{Ir}_2\text{O}_7$ has suggested a

possible reason for a similar thermomagnetic irreversibility. The authors observed through XPS studies that some amount of Ir^{5+} was found to be present in $\text{Y}_2\text{Ir}_2\text{O}_7$, probably due to a small off-stoichiometry of the sample. The double exchange between the Ir^{5+} and Ir^{4+} was said to give rise to a weak ferromagnetism. This was confirmed by Ca^{2+} doping (i.e. hole doping, which led to the creation of more Ir^{5+}), which led to an increase in the ferromagnetic component of the susceptibility. The ZFC-FC split was attributed to the inhomogeneity created by pockets of non-magnetic Ir^{5+} ions surrounded by Ir^{4+} ions. However, it is mentioned by them that μSR measurements of the compound do not show any signature of the proposed weak ferromagnetic phase, which indicates that a very small fraction of this phase is present. Such a case could be present in $\text{Eu}_2\text{Ir}_2\text{O}_7$ as well, and hole doping in the same could yield interesting results.

To check whether the ZFC-FC split obtained in $\text{Eu}_2\text{Ir}_2\text{O}_7$ corresponds to a spin-glass transition, we also measured the AC susceptibility around the transition temperature. One of the characteristics of a spin glass ground state is that the freezing temperature decreases with increasing values of applied frequency of the AC magnetic field. For $\text{Eu}_2\text{Ir}_2\text{O}_7$, the plot of χ' near the transition temperature range for different values of applied frequency is given in Figure 3.8.

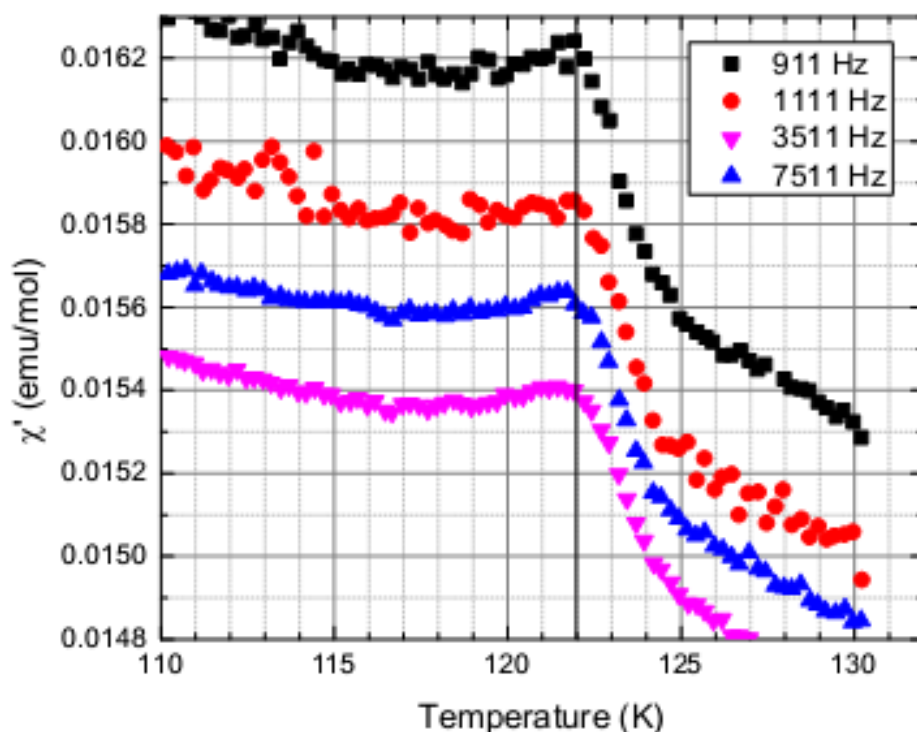


Fig 3.8 The variation of the transition temperature as a function of frequency of AC field

The peak position does not appear to be shifted over nearly a decade of applied frequencies. However, the magnitude of χ' seems to vary marginally with the applied frequency. We cannot say with certainty whether this is an intrinsic feature of the sample or an instrumental artefact. (For some of the frequencies (not shown) the magnitude of χ' did not follow the decreasing trend shown in the figure, which raises further concerns over the absolute values of χ' measured here. However, the error associated with the temperature measurements are not expected to be more than 50 mK). We plan to do a more elaborate study on the AC susceptibility over a larger temperature range in the future. However, since the peak position remains unchanged over different frequencies, the case for the existence of a spin glass phase is further weakened.

More evidence of the existence of a long-range order comes from the specific heat data for $\text{Eu}_2\text{Ir}_2\text{O}_7$ measured by us. The specific heat measured for $\text{Eu}_2\text{Ir}_2\text{O}_7$ from 2-200 K is shown in Fig. 3.9.

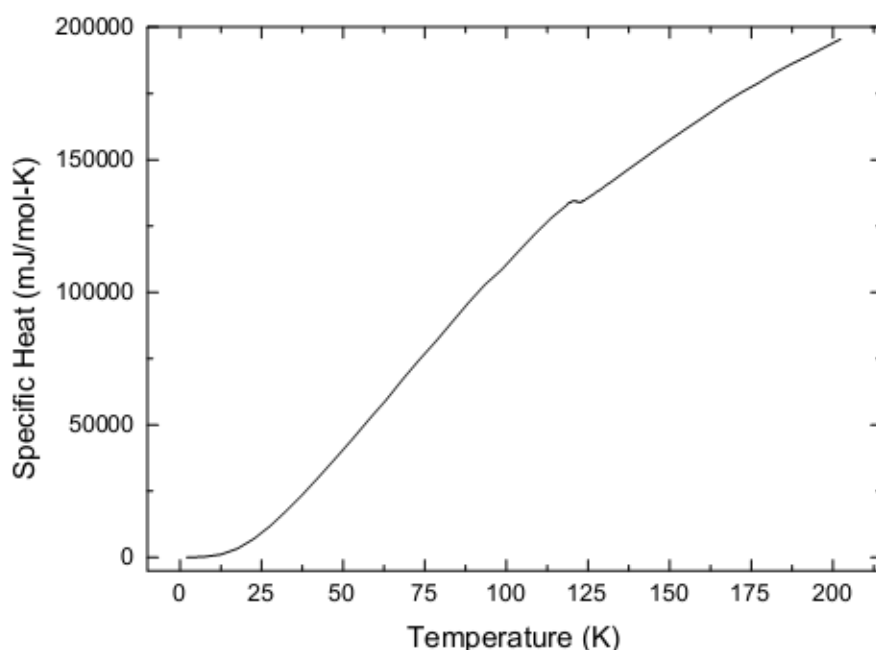


Fig 3.9 Specific heat of $\text{Eu}_2\text{Ir}_2\text{O}_7$

As can be seen from Fig. 3.9, the specific heat shows a kink near 120 K indicating that the transition that was observed in the magnetic susceptibilities is a bulk transition. The specific heat curve does not show any sign of saturation in the measurement range, implying that the Debye temperature must be higher than 200K. Measurements were also done under different values of applied magnetic field. The results are shown in Fig. 3.10.

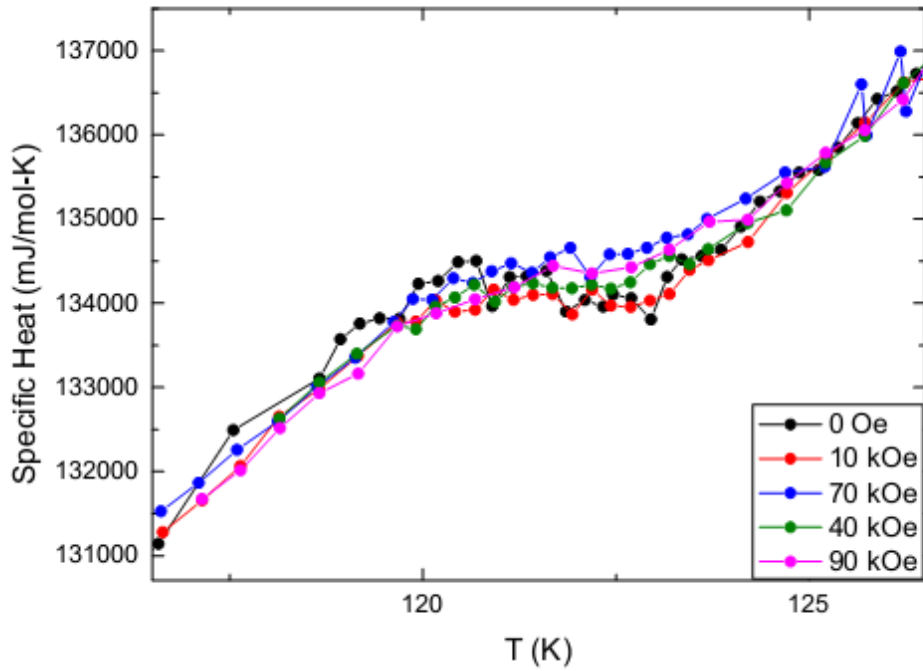


Fig 3.10 Specific heat near the transition temperature measured for different values of applied field

From the Figure 3.10, it is evident that applied magnetic fields do not affect the transition temperature, indicating a very robust nature of the magnetically ordered ground state. We tried to obtain the Debye temperature and the electronic contribution to the specific heat using the equation: $C/T = \gamma + \beta T^2$, where β is the phononic contribution to the specific heat and γ is the electronic contribution. These are given by:

$$\beta = \frac{12\pi^4 N k_B}{5T_D^3}$$

$$\gamma = \frac{\pi^2}{3} D(E_F) k_B^2 = \frac{\pi^2 N k_B^2}{2E_F}$$

Here, N is the number of atoms/ions present in the formula unit, k_B is the Boltzmann constant, T_D is the Debye temperature, and $D(E_F)$ is the electronic density of states at the Fermi level.

Thus, the density of states in a metal can be estimated from the low-temperature specific heat by determining the value of γ . Typically for non-magnetic metals (e.g., copper), the density of states and hence the associated γ values are usually small (in the range of 0.5-3 mJ/mol-K²).

The slope of the plot of C/T versus T^2 at low temperatures gives the value of β , from which the Debye temperature, T_D , can be obtained.

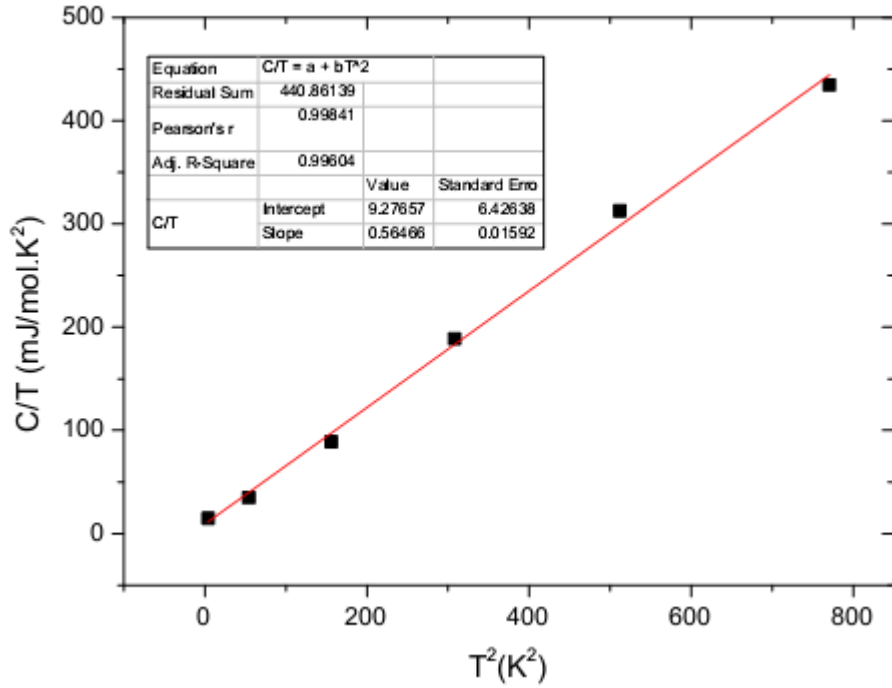


Fig 3.11 Plot of C/T versus T^2 to obtain the Debye temperature

From the values of slope and intercept summarised in the inset of Figure 3.11, we get a Debye temperature of 330 K and a γ -value of 9.3 mJ/mol.K², both of which are comparable to the values reported in previous literature (for instance, see [44]).

The γ value of Eu₂Ir₂O₇, compared to that of metals like Copper (0.69 mJ/mol.K²) [45] and Aluminium (1.35 mJ/mol.K²) [46], is considerably high. The value of γ is typically enhanced for materials with strong electronic correlations. For example in heavy fermions the gamma value can be as high as 100 – 1000 times that for copper. The obtained value of γ in Eu₂Ir₂O₇ implies the presence of moderately strong electronic correlations, which is in agreement with the theoretically predicted trend (see, for example, figure 1.8).

The obtained Debye temperature was used to calculate the phononic specific heat using the Debye Model of lattice specific heat:

$$C = N \times 9N_A K_B \left(\frac{T}{T_D}\right)^3 \int_0^{\frac{T_D}{T}} \frac{x^4 e^x}{(e^x - 1)^2} dx$$

Here $N = 11$, since there are 11 atoms per molecule of Eu₂Ir₂O₇.

The curve that we calculated using these values matched the experimental curve well up to around 30 K, but thereafter, the calculated values showed an increasing departure from the

experimental data. This could be because we considered the coefficient of the T^3 term in the specific heat expression to be the entirely due to the phononic contribution. However, the magnonic contribution to the specific heat for antiferromagnetic systems also goes as T^3 [47] and thus the β term is a sum of the phononic and magnonic contributions. Thus we underestimated the Debye temperature (since it is inversely proportional to the cube root of the coefficient β) by some amount, which could have led to the curve saturating at the Dulong-Petit limit of 25 J/mol.K at 200 K itself, unlike the measured data, where saturation is not seen up to 200 K (which is the highest measurement temperature in our experiments). However, this gives us a lower bound for the Debye temperature.

We attempted to extract the magnetic specific heat (i.e. specific heat associated with long-range ordering of the 5d electrons of Ir^{4+}) from the experimental data. The measured specific heat can be expressed as an algebraic sum of contributions due to: the electrons, the Schottky contribution due to the first excited level of Eu^{3+} , the phonons, and the magnetic ordering associated with the 5d electrons of Ir.

The electronic specific heat over the entire temperature range can be obtained from the γ value that we had gotten from the linear fitting done previously.

The Schottky contribution to specific heat arises when there are multiple discrete energy levels in the system. When the thermal energy provided by external heating is comparable to the energy gap between the levels, there is a large change in entropy for a small change in temperature and the specific heat depends more sensitively on temperature, showing up as a peak. At much lower temperatures, the thermal excitation is not sufficient to overcome the gap, whereas at much higher temperatures, all the levels are populated evenly – thus in both cases, the entropy of the system doesn't change much with temperature. In our system, there is a Schottky contribution due to the first excited state of Eu^{3+} . This was estimated taking the first excited state to be at an energy difference of 410 K.

Figure 3.12 c shows the temperature dependence of the electronic and Schottky contributions up to 200 K.

Considering the phononic contribution from the lattice next, it cannot be directly estimated since the T^3 term in $C = \alpha T + \beta T^3$ also contains the magnonic contribution, as mentioned earlier. Along with this, the phonon dispersion for $\text{Eu}_2\text{Ir}_2\text{O}_7$ is also not known. Thus a lattice template should be used to estimate the phononic contribution. A lattice template is essentially a compound with an identical lattice structure, but without any magnetic ions so that it gives only the phononic contribution. For our purpose, the pyrochlore $\text{La}_2\text{Zr}_2\text{O}_7$ was chosen as the lattice template. In figure 3.12 b, the specific heat of $\text{La}_2\text{Zr}_2\text{O}_7$ is compared with that of $\text{Eu}_2\text{Ir}_2\text{O}_7$. Far above the ordering temperature, where only the phononic contribution is most dominant,

the specific heat of $\text{La}_2\text{Zr}_2\text{O}_7$ is slightly smaller than that of $\text{Eu}_2\text{Ir}_2\text{O}_7$. This can be attributed to the difference in the molecular weights of the two compounds ($\text{La}_2\text{Zr}_2\text{O}_7$ being lighter than $\text{Eu}_2\text{Ir}_2\text{O}_7$). This difference can be accounted for if we normalise the specific heat of $\text{La}_2\text{Zr}_2\text{O}_7$ by multiplying it by a factor of 1.03, which is chosen so that the specific heats of both samples are comparable far above the ordering temperature.

As expected, both the electronic and Schottky contributions are very small compared to the phononic contribution at high temperatures. After subtracting all these contributions from the experimental data, the magnetic specific heat is obtained, which is shown in figure 3.12 d. The magnetic specific heat C_{mag} exhibits a lambda shaped anomaly at $T = 120$ K, which was expected from the long-range ordering of the 5d Ir spins. The entropy associated with the magnetic ordering is estimated by using the formula:

$$S_{\text{mag}} = \int_{T \approx 0}^{200} \frac{C_{\text{mag}}}{T} dT$$

Upon integrating, the entropy recovered saturates to a value of $R \ln 2$ near $T=120$ K, which suggests a long range ordering of the $J = \frac{1}{2}$ moments (corresponding to an effective moment of $1.73 \mu_B$) of Ir^{4+} without any moment reduction - this is in slight disagreement with the μSR studies where, though long range order is seen, the estimated size of the ordered moment is considerably lower ($0.3 \mu_B$) [11]. This difference cannot be attributed to the choice of $\text{La}_2\text{Zr}_2\text{O}_7$ as a lattice template. Though it is not an ideal choice due to the large difference in its molecular weight compared to $\text{Eu}_2\text{Ir}_2\text{O}_7$, it nevertheless supports the possibility of long range order of the Ir sublattice and also the fact that the ordered Ir moment is appreciably large.

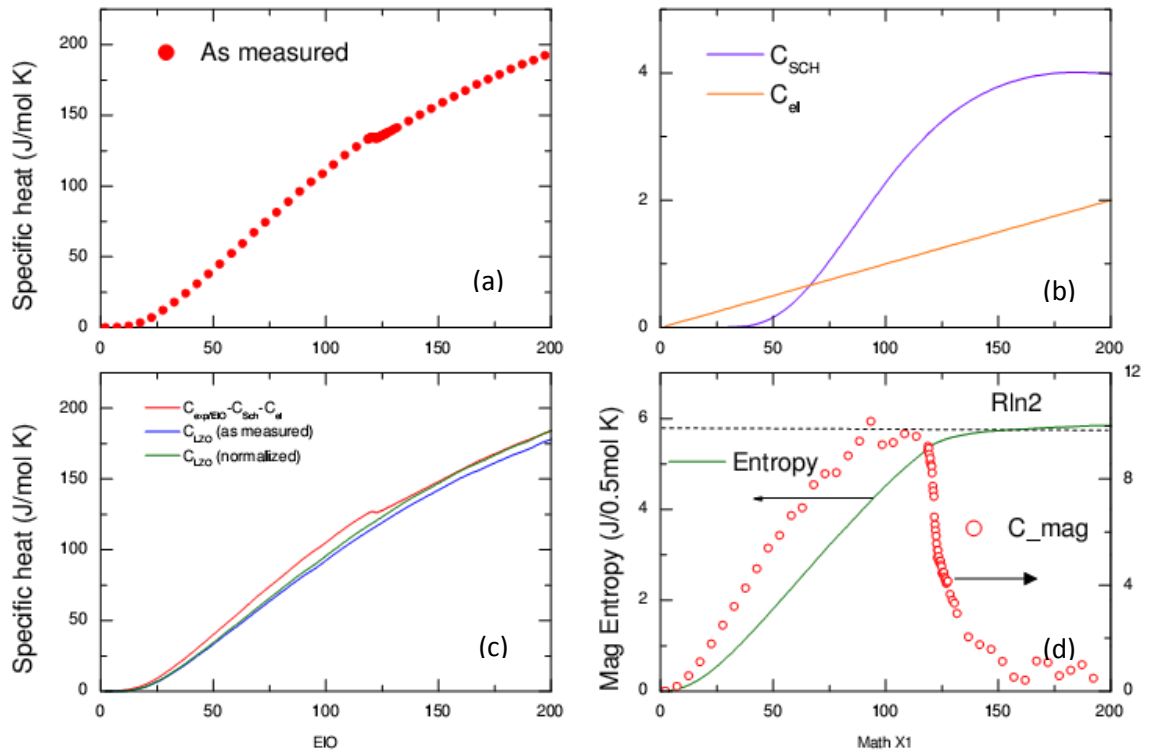


Fig 3.12 Analysis of contribution of electrons, phonons, magnons and the Schottky contribution of Eu^{3+} to the specific heat of $\text{Eu}_2\text{Ir}_2\text{O}_7$

Since 330 K is an underestimate of the Debye temperature, we tried to estimate the actual value of the same. This was done by subtracting the electronic and Schottky contributions from the experimentally obtained specific heat, and then comparing this to the phononic specific heat calculated using various trial Debye temperatures. By this procedure, a Debye temperature of roughly 560 K was obtained. While this is much higher than the values obtained by our previous estimation as well as those from other references mentioned previously, the latter calculations have not mentioned the magnetic specific heat or the Schottky contribution of the Eu ions. This value of Debye temperature compares well with that of titanate pyrochlores, which is of the order of 500 K [48].

When we attempted calculate the magnetic entropy, we saw that it saturated to a value much higher than $R\ln 2$. This was because of the large difference in the values of phononic specific heat obtained using the Debye temperature of 560 K and those obtained using $\text{La}_2\text{Zr}_2\text{O}_7$ as a lattice template. However, it must be considered here that while using the Debye model, we assumed the pyrochlore molecule to be made up of 11 identical atoms, which is not actually the case. Since the lattice template is isostructural to our compound, the phonon spectrum of our compound is expected to be similar to that of $\text{La}_2\text{Zr}_2\text{O}_7$, and hence we can conclude that the calculations done using the lattice template are more reliable than those using the Debye

model with $T_D = 560$ K. Such a usage of a lattice template is commonly done for the pyrochlores as can be seen in the references [49][50][51]

Having discussed the magnetic ground state of the parent compound, $\text{Eu}_2\text{Ir}_2\text{O}_7$, using results of three different measurement techniques, we now return to the magnetic behaviour of the rest of the series. Here, we see that the susceptibility decreases monotonically as the Bi-content increases. The difference in the ZFC and FC curves is not observed for compositions containing 10% or more Bi. The susceptibility for 5% Bi shows a ZFC-FC splitting at around 60 K. However, this splitting is not as pronounced as for $\text{Eu}_2\text{Ir}_2\text{O}_7$, which probably indicates that the magnetic ordering has weakened due to Bi-doping. This is further substantiated by the fact that this transition is completely suppressed (down to 2K) in samples with higher Bi concentration.

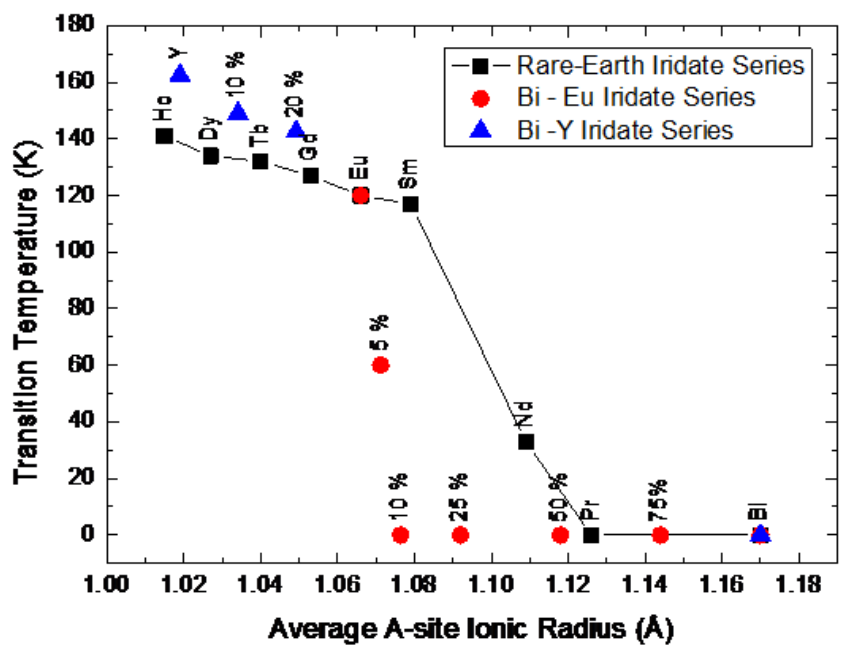
At the other end of the series, $\text{Bi}_2\text{Ir}_2\text{O}_7$ shows a temperature-independent susceptibility down to 20 K below which it rises sharply. Since the intrinsic susceptibility of this sample is relatively low, this rise could result from the presence of even trace amounts of magnetic impurities present in the starting precursors. This low temperature rise has also been observed in several other studies and is commonly referred to as the impurity driven Curie tail [15][17]. The magnitude of susceptibility for our sample at various temperatures compares well with those obtained in the reference [15].

At this point, it must be mentioned that similar studies of the effect of Bi-substitution on a pyrochlore iridate with a non-magnetic A-site, $\text{Y}_2\text{Ir}_2\text{O}_7$, have been done recently [52][37][16]. Even for this case, the ZFC-FC splitting is gradually suppressed with progressively higher concentrations of Bi added to the sample. From the data provided in reference [37], this splitting seems to completely disappear for the composition containing 80 % Bi. In the case of $\text{Eu}_2\text{Ir}_2\text{O}_7$, the addition of Bi suppresses the transition much more rapidly as opposed to the case of $\text{Y}_2\text{Ir}_2\text{O}_7$. In $\text{Eu}_2\text{Ir}_2\text{O}_7$, 10 % Bi doping is enough to completely suppress the magnetic transition, whereas it takes 80 % of Bi content to do the same in $\text{Y}_2\text{Ir}_2\text{O}_7$. At this point, the reason behind this is not well understood.

The magnetic behaviour across the Bi-Eu series gives further proof of the fact that changing the average A-site radius through Bi^{3+} substitution in $\text{Eu}_2\text{Ir}_2\text{O}_7$, and even $\text{Y}_2\text{Ir}_2\text{O}_7$, is different from changing only the radius of the A-site ion across the rare-earth series. In the latter case, the metal-insulator transition and magnetic transition is found to move to lower temperatures as the series progresses from $A = \text{Y}$ (smallest ionic radius) to $A = \text{Pr}$ (largest ionic radius) [8]. In the Bi-doped series, however, the ionic radius is not the only factor that is changing. As hinted in the observations regarding the lattice parameters, the 5d-6s overlap between the Bi

and Ir ions affect the magnetic transition as well. This is further corroborated by the electrical transport property measurements discussed in the next section.

We attempt to compare the transition temperatures corresponding to average ionic radii of our synthesised series with the rare-earth series [8] and with the $Y_{2-x}Bi_xIr_2O_7$ series [16] in Table 3.5 and Figure 3.13



Compound	Average A-site Ionic Radius (Å)	Transition Temperature (K)
Ho ₂ Ir ₂ O ₇	1.015	141
Y ₂ Ir ₂ O ₇	1.019	162.5
Dy ₂ Ir ₂ O ₇	1.027	134
Bi _{0.2} Y _{1.8} Ir ₂ O ₇	1.034	149
Tb ₂ Ir ₂ O ₇	1.04	132
Bi _{0.4} Y _{1.6} Ir ₂ O ₇	1.049	142.5
Gd ₂ Ir ₂ O ₇	1.053	127
Eu₂Ir₂O₇	1.066	120
5% Bi	1.071	60
10% Bi	1.076	-
Sm ₂ Ir ₂ O ₇	1.079	117
25% Bi	1.092	-
Nd ₂ Ir ₂ O ₇	1.109	33
50% Bi	1.118	-
Pr ₂ Ir ₂ O ₇	1.126	-
75% Bi	1.144	-

$\text{Bi}_2\text{Ir}_2\text{O}_7$	1.17	-
------------------------------------	------	---

Table 3.5 Ionic radii for A-site and magnetic transition temperature for the $\text{A}_2\text{Ir}_2\text{O}_7$ (A-rare-earth ion) series and the Bi-Eu series

From the above comparison, it is evident that Bi doping at the Eu (or Y) site doesn't simply affect the magnetic ground state via the A-site radius, even though Bi^{3+} is isovalent with the rare earth ions it is substituting. This situation can be contrasted with the effect of carrier doping on magnetism in the pyrochlore iridates. Carrier doping was attempted in $\text{Nd}_2\text{Ir}_2\text{O}_7$ in the reference [53]. In the undoped $\text{Nd}_2\text{Ir}_2\text{O}_7$ samples, the ground state itself is sensitively dependent on details of sample preparation. Therefore the effect of carrier-doping in $\text{Nd}_2\text{Ir}_2\text{O}_7$ is not very clear. On the other hand, in the case of Ca^{2+} doping in $\text{Y}_2\text{Ir}_2\text{O}_7$, it was found that on adding holes, the transition shifts to higher temperatures [43]. Thus, the effect of hole-doping in iridates is different from that of Bi^{3+} doping, which tends to suppress the magnetic transition. It would be interesting to see the results of electronic-doping in the pyrochlore iridates.

Another feature in the M-T measurements for all samples except $\text{Bi}_2\text{Ir}_2\text{O}_7$ is that the magnetic susceptibility shows a temperature-dependence very similar to that obeyed by the van Vleck susceptibility (see figure 3.6). Since Eu^{3+} is present in all samples except $\text{Bi}_2\text{Ir}_2\text{O}_7$, we tried to subtract the van Vleck susceptibility due to the corresponding amount of Eu^{3+} (taking $\lambda = 400$ K) for each sample. The resultant curves are shown in Fig 3.14.

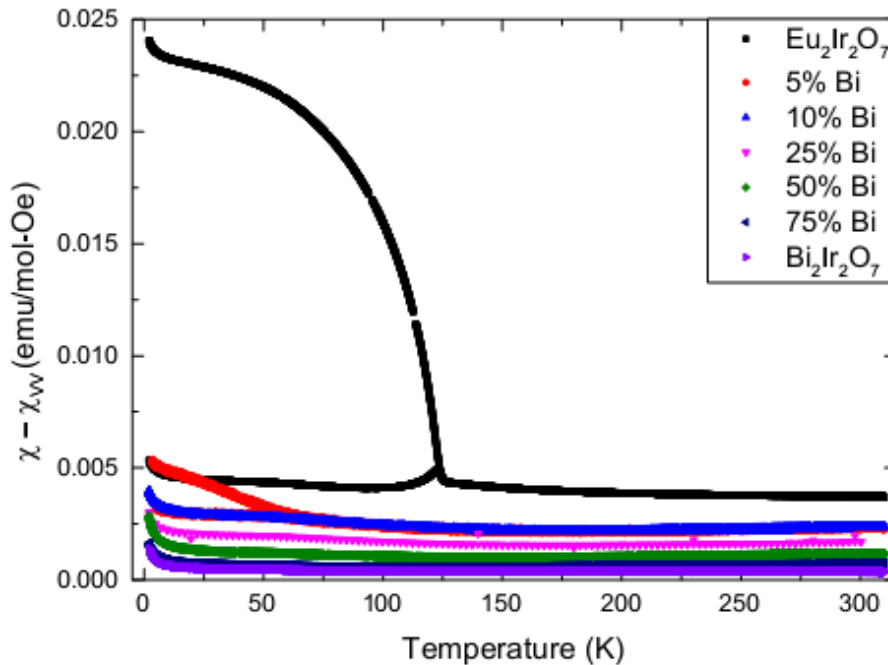


Fig 3.14 Susceptibility obtained after removing the van Vleck contribution of Eu^{3+} for each sample

It can be seen that after removing the van Vleck contribution from $\text{Eu}_2\text{Ir}_2\text{O}_7$, the susceptibility above 120 K becomes nearly temperature independent. The same can be inferred for the other samples, i.e., their susceptibilities after subtracting the van Vleck contribution exhibit a nearly temperature-independent behavior. The weak temperature dependence that still remains after subtraction (not very noticeable on the scale of the plot) can easily arise from an error in estimating the van Vleck contribution, and in particular, the value of λ . This is because while the energy difference between the levels is calculated using the theory of spin-orbit coupling, the splitting of levels is not a simple case of S-O coupling induced splitting. The crystal field present influences the energy levels as well.

These nearly temperature-independent susceptibility values are summarised in table 3.6 below. Thus, it can be concluded that in the paramagnetic range all samples exhibit Pauli paramagnetic behaviour with somewhat enhanced values of the Pauli susceptibility which indicates the presence of moderately strong electronic correlations: a conclusion independently arrived at from the specific heat data discussed before. It should be noted here that after subtracting the contribution of Eu^{3+} , the curves still don't fall on each other, but are dc-shifted. This seems to suggest that the Pauli paramagnetism decreases with increasing Bi-content.

Compound	χ_p (10^{-3} emu/mol-Oe)
$\text{Eu}_2\text{Ir}_2\text{O}_7$	3.72
5% Bi	2.40
10% Bi	2.36
25% Bi	1.71
50% Bi	1.19
75% Bi	0.70
$\text{Bi}_2\text{Ir}_2\text{O}_7$	0.38

Table 3.6 Pauli paramagnetic susceptibility values for the Bi-Eu series of compounds

The curves were also analysed by normalising the susceptibility with the Europium-content. This yields a plot as shown in Figure 3.15.

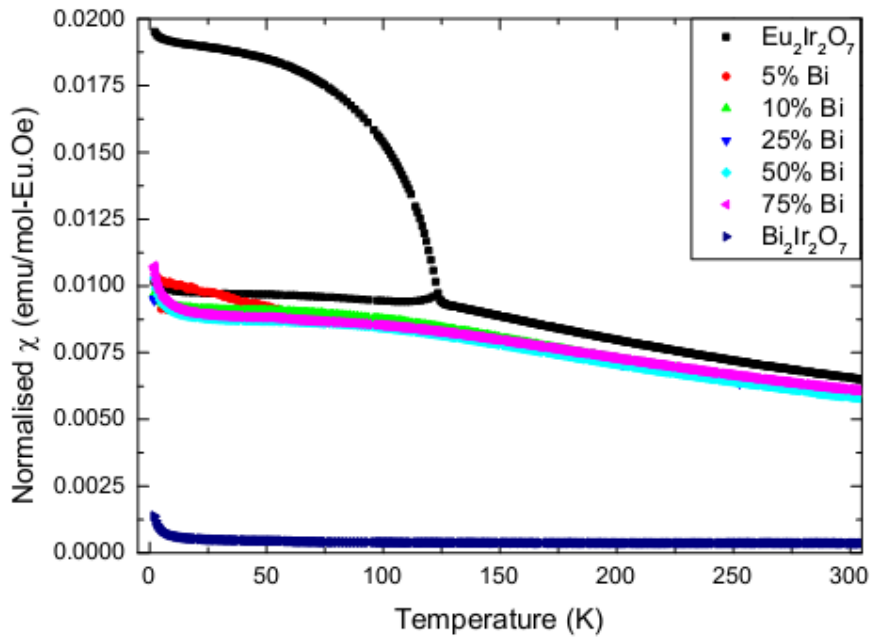


Fig 3.15 The magnetic susceptibility of the series normalised by the Eu-content

Upon normalising the susceptibilities by the Eu content in the samples (Figure 3.15), it is observed that the intermediate compositions show overlapping susceptibilities. Normalising the susceptibility by the Eu content essentially means that we divide the molar susceptibility by the number of moles of Europium present per mole of the sample. This quantity would be same for two samples with different Eu concentration only in the absence of any other contribution to the susceptibility, or in the case that the other contributions are much smaller than that of Eu^{3+} . For this case, we see that all the intermediate compositions nearly overlap on each other and lie between the two ends of the series. This must imply that the Pauli paramagnetism in the Bi-containing samples is not only very small compared to the van Vleck paramagnetism, but also smaller than that in $\text{Eu}_2\text{Ir}_2\text{O}_7$ (since the curve for $\text{Eu}_2\text{Ir}_2\text{O}_7$ is not overlapping with the others). It could be possible that the presence of Bi is decreasing the electronic density of states, resulting in a lowered Pauli susceptibility. It would be interesting to measure the specific heat of these samples and see if the γ value reflects a similar trend.

The M versus H measurements yield the following plots at 300K:

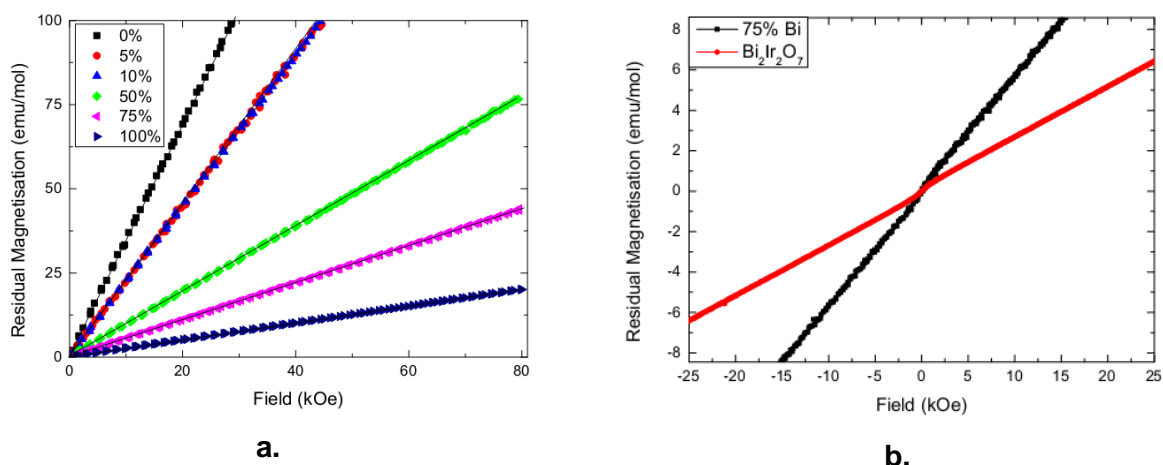


Fig 3.16 a. Residual magnetisation ($M_{\text{expt}} - M_{\text{Eu}}$) versus H at 300 K fitted to straight lines b. $\text{Bi}_2\text{Ir}_2\text{O}_7$ and 75% Bi showing non-linear residual magnetisation curves at 300 K

At 300 K, the M-H behaviour of all the samples except the 75% Bi sample and $\text{Bi}_2\text{Ir}_2\text{O}_7$ is a straight line with no visible hysteresis, indicating a paramagnetic behaviour. As for the 75% Bi sample and $\text{Bi}_2\text{Ir}_2\text{O}_7$, though there is no hysteresis loop, the curves are not exactly linear. There is observed to be some kind of inflection of the magnetisation curve at zero field. Though the reason for this is not known, the non-linear M-H curve has been reported in the reference [15] as well.

The molar magnetic moment is seen to decrease with increasing Bismuth content. On fitting straight lines to the molar magnetic moment after subtracting the van Vleck susceptibility, the slope (which would yield the Pauli paramagnetic susceptibility) was compared to the Pauli paramagnetic susceptibility values obtained from the M-T plots in Fig 3.14. The comparison is summarised in the table below:

Pauli paramagnetic susceptibility, χ_0 (emu/mol)		
Compound	M-T curve	M-H curve
$\text{Eu}_2\text{Ir}_2\text{O}_7$	0.00344	0.00369
5% Bi	0.00225	0.00239
10% Bi	0.00224	0.00228
25% Bi	0.00238	-
50% Bi	0.000964	0.001168
75% Bi	0.000548	0.000711
$\text{Bi}_2\text{Ir}_2\text{O}_7$	0.000251	0.000364

Table 3.7 Comparison of Pauli paramagnetic susceptibility values from M-H and M-T measurements for the Bi-Eu series of compounds

The values are comparable in both cases, except for the sample with 25% Bi, for which M-H measurements were not made.

At 2K, none of the compounds showed saturation of the magnetisation up to the highest applied fields or magnetic hysteresis. Even at 2 K the 75% Bi sample and $\text{Bi}_2\text{Ir}_2\text{O}_7$ show a non-linear dependence of the moment on the applied field, which is plotted in Fig 3.17 b. Assuming that this non-linearity is arising due to a trace amount of paramagnetic impurity in the sample, (as assumed for explaining the low temperature rise in the magnetic susceptibility) we tried fitting the M versus H data at 2 K to a Brillouin function, which did not yield a satisfactory fit. In reference [17], where studies were carried out on single crystalline samples, a similar behaviour is reported. The authors in this report argued (based on other complementary measurements) that $\text{Bi}_2\text{Ir}_2\text{O}_7$ is close to a magnetic instability. This non-linearity becomes less and less evident as the composition goes towards $\text{Eu}_2\text{Ir}_2\text{O}_7$.

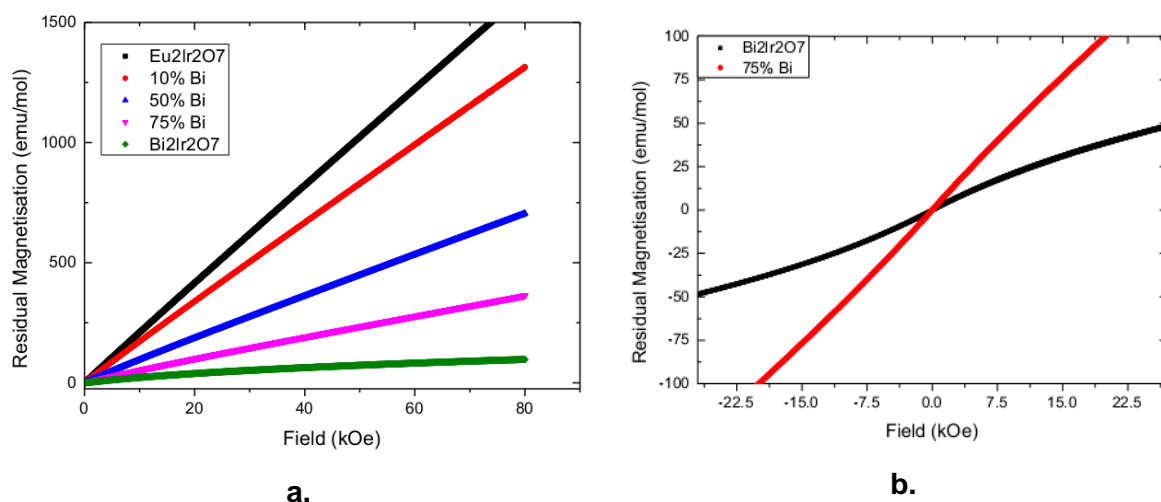


Fig 3.17 a. M-H curves of some of the samples at 2K **b.** $\text{Bi}_2\text{Ir}_2\text{O}_7$ and 75% Bi showing non-linear M-H curves at 2 K

3.4 Electrical Transport Measurements

The electrical resistivity data of some of our samples are summarised in the figure 3.18.

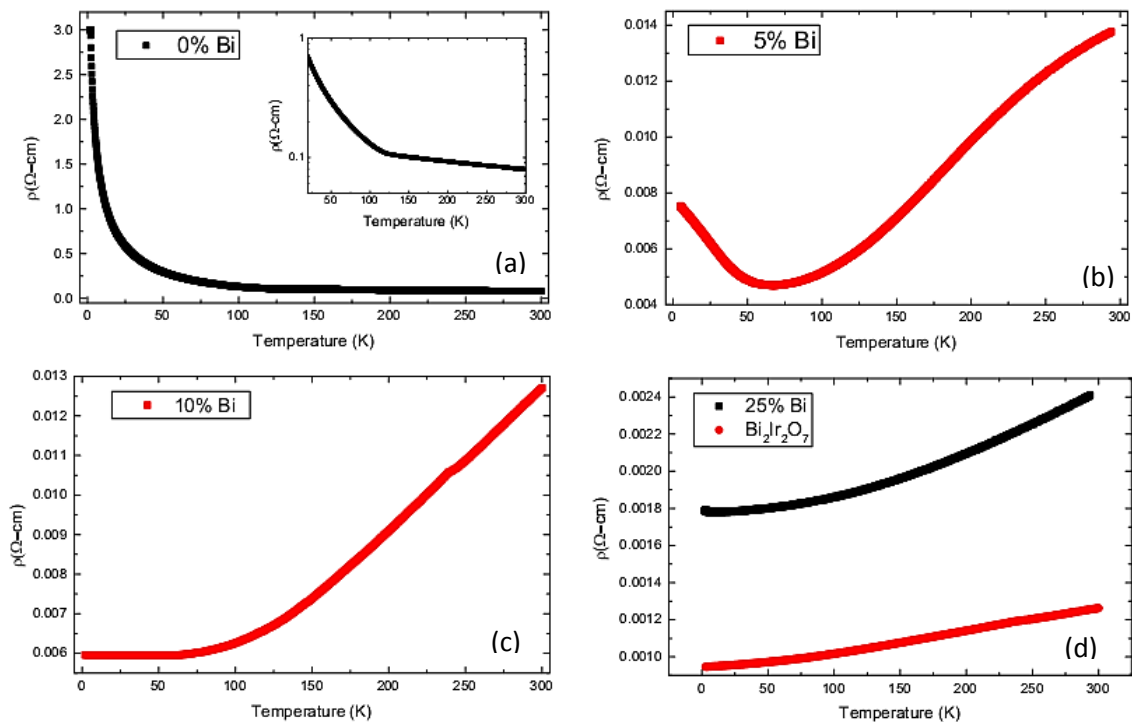


Fig 3.18 The resistivities of some of the samples plotted against temperature

For the parent compound, $\text{Eu}_2\text{Ir}_2\text{O}_7$. Upon cooling below the room temperature the resistivity increases slowly, exhibits a kink near $T=120$ K (see inset of Fig 3.18 a) marking the onset of the long range magnetic ordering of the Ir^{4+} sublattice. Below 120 K, the resistivity shows a pronounced increase. This behaviour is often characterised as a transition from a metal-like resistivity in the paramagnetic state to an insulating behaviour in the ordered state. The resistivity behaviour observed by us is in qualitative agreement with that reported in reference [8]. Qualitative comparison of our data with the data in this reference shows that while the magnitude of resistivity matches near room temperatures, the rise for the resistivity in reference [8] at low temperatures is nearly three orders of magnitude more than our sample.

Considering the slope of the resistivity $d\rho/dT$ for our sample, we observe that this slope is negative throughout the temperature range, but its magnitude increases significantly at 120 K. Comparing this with another case of resistivity measurement on single crystals [14], $d\rho/dT$ is found to be a small negative for temperatures higher than 120 K and positive below it. In some other works, ([8],[54]. The report in ref [50] is on single-crystalline samples.) the sign of $d\rho/dT$ is reported to be negative both above and below the transition temperature, in agreement with our work. The above comparisons suggest that there is a sample dependence

of the electrical transport properties for this compound. Nonetheless, there is an overall agreement on one point – that there is a significant change in the resistivity behaviour at $T = 120$ K. The reason for this sample dependence is not well understood. In order to address this question, we investigated an off-stoichiometric sample to see if its properties reflected such a sample dependence. We observed that the off-stoichiometric sample ($\text{Eu}_{2.02}\text{Ir}_{1.98}\text{O}_{6.99}$) showed a positive slope at higher temperatures, unlike the nominally stoichiometric sample. Thus the sample dependence visible in the various studies could be arising from different stoichiometries of the compound. This needs to be looked into in greater detail. Another possible reason for different samples showing such a difference in the resistivity behaviour could be due to the realisation of a topological insulating state in them, as predicted from theoretical calculations. Since such a state is conducting on the surface but insulating in its bulk, its electrical transport properties could vary with variation in the surface structure of these compounds, which depends on details of sample preparation such as pressing them into pellets at different pressures, for different durations and so on. This hypothesis could be investigated by studying the properties of samples prepared by a controlled synthesis under different preparation conditions.

Interestingly, with just 5% of Bi-doping in $\text{Eu}_2\text{Ir}_2\text{O}_7$, a very significant change in the behaviour is observed. Upon cooling the sample, the resistivity decreases steeply ($d\rho/dT > 0$). At around 60 K, the slope of the resistivity gradually changes its sign and upon further cooling, the resistivity increases with decreasing temperatures. At 300 K, the magnitude of the resistivity of the 5 % Bi doped sample is an order of magnitude smaller than that of the undoped $\text{Eu}_2\text{Ir}_2\text{O}_7$, and this difference becomes even more pronounced at lower temperatures. This change of the resistivity behaviour from $\text{Eu}_2\text{Ir}_2\text{O}_7$ to the 5 % Bi doped sample is possibly related to the change of the electronic band structure due to the 5d-6s overlap, which was previously alluded to in the context of lattice parameter variation and magnetic behaviour.

For the 10% Bi sample, the kind of upturn seen in the 5% Bi sample is not seen. However, the resistivity curve flattens below 60 K. The 25% sample shows a resistivity which decreases with decreasing temperature. There is a slight flattening of the curve below roughly 20 K, and then a rise below 6 K. Both the 50 and 75% Bi curves (not shown in Fig 3.18) also show a slight upturn of the resistivity below 15 K, but a metallic behaviour above 15 K. The resistivity of $\text{Bi}_2\text{Ir}_2\text{O}_7$ shows no such flattening or upturns.

The resistivity normalised by the resistivity at 300 K ($\rho/\rho(300\text{K})$) is plotted in the following figure.

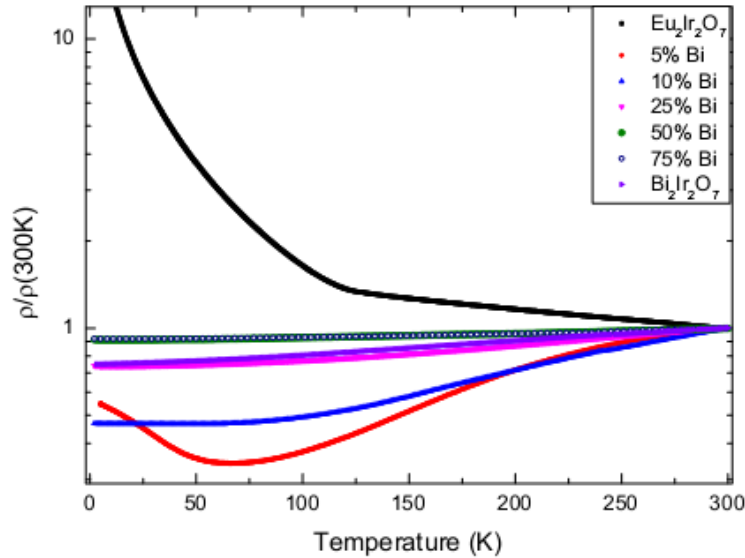


Fig 3.19 The normalised resistivities plotted against temperature

With increasing bismuth concentration, the absolute values of resistivity also decrease, which is as expected, since $\text{Bi}_2\text{Ir}_2\text{O}_7$ shows a completely metallic behaviour as opposed to $\text{Eu}_2\text{Ir}_2\text{O}_7$, which shows an M-I transition. The resistivity of $\text{Bi}_2\text{Ir}_2\text{O}_7$ is observed to be higher than that of 75% Bi, though. On plotting the normalised values of resistivity $\rho/\rho(300\text{ K})$, an unusual trend is observed: $\rho/\rho(300\text{ K})$ data for the 50 and 75% Bi samples is higher in magnitude than that for $\text{Bi}_2\text{Ir}_2\text{O}_7$. However, for 25, 10 and 5 % Bi sample $\rho/\rho(300\text{ K})$ is smaller than for $\text{Bi}_2\text{Ir}_2\text{O}_7$; i.e., starting from the $\text{Bi}_2\text{Ir}_2\text{O}_7$, upon substituting Eu for Bi $\rho/\rho(300\text{ K})$ first increases before decreasing again above 75% Eu substitution. Normally for metallic samples the ratio, $\rho(2\text{ K})/\rho(300\text{ K})$ is associated with the amount of disorder in the sample. The substitution of Eu for Bi in $\text{Bi}_2\text{Ir}_2\text{O}_7$ is expected to increase the disorder in the sample which could possibly be related to the increase in the $\rho/\rho(300\text{ K})$ values for the 75% Bi and the 50% Bi samples. On the other hand, the behaviour of the samples towards the $\text{Eu}_2\text{Ir}_2\text{O}_7$ end will be governed by the 5d-6s overlap.

Once again, we can compare our findings with those obtained in the study of Bi doping in $\text{Y}_2\text{Ir}_2\text{O}_7$ [37]. Even there, it is observed that $\text{Y}_2\text{Ir}_2\text{O}_7$, which exhibits a Mott insulating ground state, turns increasingly metallic on addition of Bi. An upturn is observed in the resistivity for samples with less than 20% of Bi. For higher Bi concentrations, this upturn disappears and the samples show metallic behaviour. As seen in the case of magnetic susceptibility, the change in Y-Bi series is much more gradual compared to those in the Eu-Bi series. It would be interesting to investigate why Bi-doping doesn't affect the ground state of $\text{Eu}_2\text{Ir}_2\text{O}_7$ and $\text{Y}_2\text{Ir}_2\text{O}_7$ at the same rate. A possible reason is that $\text{Eu}_2\text{Ir}_2\text{O}_7$ is closer to a metallic ground state than $\text{Y}_2\text{Ir}_2\text{O}_7$ is, therefore in a solid solution series with metallic $\text{Bi}_2\text{Ir}_2\text{O}_7$, the transition for the Eu-Bi series would be much faster than for the Y-Bi series.

Considering the low temperature behaviour of the samples, the resistivities of $\text{Eu}_2\text{Ir}_2\text{O}_7$ and 5% Bi can be fit to the Variable Range Hopping Model (VRH), which is a relation that describes conduction in a highly localised electronic system. The relation between temperature and resistivity for the VRH is given by the equation:

$$\rho(T) = \rho_0 e^{\left(\frac{T_0}{T}\right)^{\frac{1}{4}}}$$

Thus, a plot of $\ln(\rho/\rho(300\text{K}))$ versus $T^{-1/4}$ should give a straight line at low temperatures. These plots are observed to exhibit linear behaviour for $\text{Eu}_2\text{Ir}_2\text{O}_7$ and 5% Bi up to temperatures of 4 K and 10 K respectively, as shown in figure 3.20. Linearity over a similar temperature range has been seen in single crystalline samples of $\text{Eu}_2\text{Ir}_2\text{O}_7$ in the reference [14]

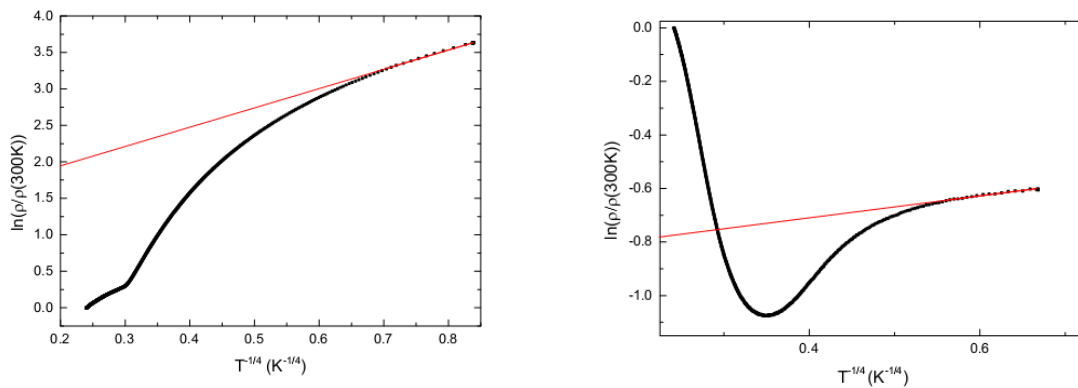


Fig 3.20 The resistivities of $\text{Eu}_2\text{Ir}_2\text{O}_7$ and 5% Bi fitted to the VRH model

This implies that at very low temperatures, charge carriers are localised for both $\text{Eu}_2\text{Ir}_2\text{O}_7$ and the 5% Bi sample. As Bi content increases, the curves can no longer be fit to the VRH model. Interestingly, according to reference [8], among the rare earth iridates, $\text{Eu}_2\text{Ir}_2\text{O}_7$ is reported to be the only compound for which the resistivity below the MIT can be modelled using VRH.

A thorough analysis of the behaviour and implications of the resistivity for all the samples in the Bi-Eu series has not yet been done. This is because of several problems faced while performing measurements, mainly related to the electrical contacts on the sample. We plan to do a detailed analysis in the future. However, looking at the data obtained so far, it can be concluded that the resistivity data corroborates the features observed in the magnetic data. The metal-insulator transition seen in the resistivity behaviour seems to be very strongly correlated with the magnetic transition in not just this series, but also in the Y-Bi iridate series studied in [37]. A deeper look into the transport properties, not just electrical, but also magnetotransport as well as thermal transport could yield valuable information about the mechanism behind these transitions and the factors driving them.

3.5 Effect of Off-Stoichiometry in $\text{Eu}_2\text{Ir}_2\text{O}_7$

As mentioned earlier, samples with an off-stoichiometry of 2% had been obtained in a pyrochlore phase. Magnetic and electric transport properties were measured on one of these— $\text{Eu}_{2.02}\text{Ir}_{1.98}\text{O}_{6.99}$ – to see the role of off-stoichiometry in governing the behaviour of pyrochlore iridates. The results are summarised in the figures below:

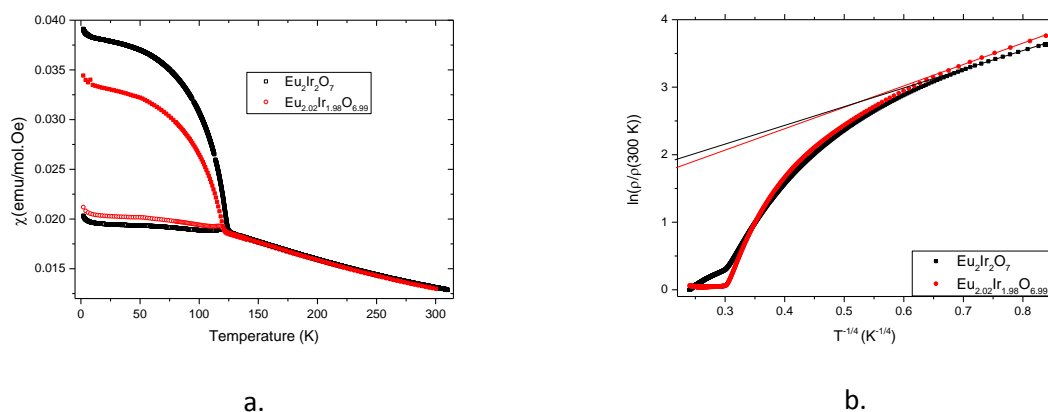


Fig 3.21 a. Magnetic susceptibility of $\text{Eu}_2\text{Ir}_2\text{O}_7$ and $\text{Eu}_{2.02}\text{Ir}_{1.98}\text{O}_{6.99}$ as a function of temperature. **b.** $\ln(\rho/\rho(300\text{K}))$ plotted against $T^{-1/4}$ in accordance with the Variable Range Hopping Model.

The magnetic susceptibility is lesser for the off-stoichiometric compound below the transition temperature. Interestingly, the magnetic transition temperature of the off-stoichiometric sample is found to be 118 K as opposed to 123 K for the stoichiometric sample.

The resistivities are compared in Figure 3.21 b. As mentioned previously, in the off-stoichiometric sample, the $d\rho/dT$ changes sign below 120 K, whereas the sign of $d\rho/dT$ remains negative over the entire temperature range for the nominally stoichiometric sample.

Since reference [14] involves a study on off-stoichiometric crystals, it is worth looking at their results for $\text{Eu}_2\text{Ir}_2\text{O}_7$. They observe that off-stoichiometry in any direction leads to reduction in resistivity i.e. both Eu-rich as well as Ir-rich compounds were seen to have lesser resistivity than the pure compound. This was attributed to the generation of excess charge carriers due to off-stoichiometry. The effect of off-stoichiometry on magnetic behaviour has not been discussed, but if their reasoning is true, then the excess charge carriers should also contribute to the Pauli paramagnetic susceptibility and enhance it for the off-stoichiometric compounds. This is not observed in our magnetic data – the two curves overlap in the paramagnetic region.

A more controlled study on off-stoichiometric samples, where samples with an equal excess and deficit of Eu/Ir are compared to the pure sample would probably shed more light on the effect of off-stoichiometry on the ground state of $\text{Eu}_2\text{Ir}_2\text{O}_7$.

Conclusions and Outlook

We have successfully synthesised two pyrochlore iridates, $\text{Bi}_2\text{Ir}_2\text{O}_7$ and $\text{Eu}_2\text{Ir}_2\text{O}_7$, and a series of compounds with intermediate compositions. Physical property measurements done on these samples reveal that the ground states of the two compounds are very different and the intermediate compositions do not show simple trends like those shown by the rare-earth iridate series. It is seen that the ground state of $\text{Eu}_2\text{Ir}_2\text{O}_7$ is very sensitive to even minor doping by Bi. In fact, it is at the $\text{Eu}_2\text{Ir}_2\text{O}_7$ end of the series that the most interesting behaviour is displayed. As we move closer to $\text{Bi}_2\text{Ir}_2\text{O}_7$, the trends such as lattice parameter variation, and magnetic and transport properties follow the expected behaviour.

Samples very close in composition to $\text{Eu}_2\text{Ir}_2\text{O}_7$ (with 5 and 10% Bi doping respectively) do not follow the linear lattice parameter rise displayed by the rest of the series. A possible reason behind this could be overlapping between the 6s lone pair of Bi and the 5d orbitals of Iridium. This could also be the reason behind the magnetic transition temperature of the Bi-Eu series not following the monotonically decreasing pattern seen in the rare-earth iridate series. Such an overlap could explain the electrical transport properties as well, which corroborate with the magnetic properties of the series.

In particular, for the compound $\text{Eu}_2\text{Ir}_2\text{O}_7$, our AC susceptibility and specific heat results imply the absence of a spin-glass phase below the transition temperature. However, our specific heat results point at a $J=1/2$ state for the Ir^{4+} ions without any reduction in the effective magnetic moment, which is in slight disagreement the findings of μSR reports on the compound. Apart from this, the electronic specific heat value suggests the presence of moderate correlations, which is in keeping with the theoretically predicted trends. Specific heat measurements on the other samples in the series, especially the 5% Bi composition and $\text{Bi}_2\text{Ir}_2\text{O}_7$ would shed more light on the magnetic ground state of the Ir sublattice and how it is affected by Bi-doping. AC susceptibility studies across a wider temperature range would also yield information on the interactions present in the samples of this series.

The magnetic property measurements imply that in the paramagnetic phase the Ir 5d electrons are delocalised in all the compounds, giving a Pauli paramagnetic susceptibility. However, the magnitude of this susceptibility is not the same for all compounds of the series – it is in fact found to decrease with increasing Bi content, implying that Bismuth substitution has an effect not just on the ionic radius of the A-site but probably also on factors like electronic density of states at the Fermi level.

The thermomagnetic irreversibility observed at one end of the series – in $\text{Eu}_2\text{Ir}_2\text{O}_7$, at 120 K – is suppressed down to 60 K with just 5% of Bismuth substitution, and is completely suppressed after 10% of Bismuth doping, suggesting that the ground state of $\text{Eu}_2\text{Ir}_2\text{O}_7$ is highly unstable to even minor perturbations.

The resistivity behaviour of the series also shows interesting features. The 5% Bi doped compound shows a metal-insulator transition at 60 K, accompanying the ZFC-FC splitting seen in magnetic measurements. This further strengthens the possibility of existence of some kind of correlation between the metal-insulator transition and the magnetic transition.

Interesting insights into the effect of Bismuth on the physical properties of $\text{Eu}_2\text{Ir}_2\text{O}_7$ might be obtained by studying compounds very close to the Eu composition. Currently, the physical properties of a sample with 1%-Bi composition are being investigated.

Studies on the effect of off-stoichiometry on $\text{Eu}_2\text{Ir}_2\text{O}_7$ seem to imply that though off-stoichiometry might not affect the low-temperature behaviour of $\text{Eu}_2\text{Ir}_2\text{O}_7$ to a great extent, it appears to have some effect on the transition temperature. However, more investigation needs to be done in this regard to come to a more definitive conclusion regarding off-stoichiometry.

Since neutron scattering cannot yield much information about these compounds, much of the future research towards understanding their puzzling properties will partly rely on systematic investigations of bulk properties through structural perturbations which could be extrinsic (e.g., applied pressure) or chemically (e.g., by substitution at the A-site) as was attempted in this work.

Bibliography

- [1] J. S. Gardner, M. J. P. Gingras, and J. E. Greedan, "Magnetic pyrochlore oxides," *Rev. Mod. Phys.*, vol. 82, pp. 53–107, 2010.
- [2] X. Wan, A. M. Turner, A. Vishwanath, and S. Y. Savrasov, "Topological semimetal and Fermi-arc surface states in the electronic structure of pyrochlore iridates," *Phys. Rev. B - Condens. Matter Mater. Phys.*, vol. 83, pp. 1–9, 2011.
- [3] X. Wan, A. Turner, A. Vishwanath, and S. Y. Savrasov, "Electronic Structure of Pyrochlore Iridates: From Topological Dirac Metal to Mott Insulator," *arXiv Prepr. arXiv1007.0016*, pp. 1–9, 2010.
- [4] P. Clancy, Z. Yamani, R. Donabergner, and Y. J. Kim, "Searching for Magnetic Order in the Pyrochlore Iridate $Y_2Ir_2O_7$," vol. 214434, pp. 2–3, 2012.
- [5] W. Witczak-Krempa, A. Go, and Y. B. Kim, "Pyrochlore electrons under pressure, heat, and field: Shedding light on the iridates," *Phys. Rev. B - Condens. Matter Mater. Phys.*, vol. 87, pp. 1–7, 2013.
- [6] J. E. Greedan, "Geometrically frustrated magnetic materials," *J. Mater. Chem.*, vol. 11, pp. 37–53, 2001.
- [7] M. A. Subramanian, G. Aravamudan, and G. V. S. Rao, "Oxide Pyrochlores - A Review," *Prog. Solid State Chem*, vol. 15, pp. 55–143, 1983.
- [8] K. Matsuhira, M. Wakeshima, Y. Hinatsu, and S. Tagaki, "Metal-Insulator Transition in Pyrochlore Oxides $Ln_2Ir_2O_7$," *J. Phys. Soc. Japan*, vol. 80, no. 9, p. 094701, 2011.
- [9] P. Baker, J. Möller, F. Pratt, and W. Hayes, "Weak magnetic transitions in pyrochlore $Bi_2Ir_2O_7$," *Phys. Rev. B*, pp. 1–5, 2013.
- [10] R. D. Shannon, "Revised effective ionic radii and systematic studies of interatomic distances in halides and chalcogenides," *Acta Crystallogr. Sect. A*, vol. 32, no. 5, pp. 751–767, 1976.
- [11] S. Zhao, J. M. MacKie, D. E. MacLaughlin, O. O. Bernal, J. J. Ishikawa, Y. Ohta, and S. Nakatsuji, "Magnetic transition, long-range order, and moment fluctuations in the pyrochlore iridate $Eu_2Ir_2O_7$," *Phys. Rev. B - Condens. Matter Mater. Phys.*, vol. 83, 2011.
- [12] S. M. Disseler, "Direct Evidence for the 'All-in/All-out' Magnetic Structure in the Pyrochlore Iridates from μ SR," *Phys. Rev. B*, vol. 89, no. 14, p. 140413, 2014.
- [13] E. Lefrançois, V. Simonet, R. Ballou, E. Lhotel, S. Kodjikian, P. Lejay, P. Manuel, D. Khalyavin, and L. C. Chapon, "Anisotropy tuned magnetic order in pyrochlore iridates," *arXiv Prepr. arXiv1502.00787*, pp. 1–6, 2015.
- [14] J. J. Ishikawa, E. C. T. O'Farrell, and S. Nakatsuji, "Continuous transition between antiferromagnetic insulator and paramagnetic metal in the pyrochlore iridate $Eu_2Ir_2O_7$," *Phys. Rev. B - Condens. Matter Mater. Phys.*, vol. 85, 2012.

- [15] K. Sardar, S. C. Ball, J. D. B. Sharman, D. Thompsett, J. M. Fisher, R. a P. Smith, P. K. Biswas, M. R. Lees, R. J. Kashtiban, J. Sloan, and R. I. Walton, "Bismuth iridium oxide oxygen evolution catalyst from hydrothermal synthesis," *Chem. Mater.*, vol. 24, pp. 4192–4200, 2012.
- [16] T. Medina Fernandez, "Magnetic Characterization of $Y(2-x)Bi_xIr_2O_7$: A Muon Spin Rotation/Relaxation and Susceptibility Study," 2014.
- [17] T. F. Qi, O. B. Korneta, X. Wan, L. E. DeLong, P. Schlottmann, and G. Cao, "Strong magnetic instability in correlated metallic $Bi_2Ir_2O_7$," *J. Phys. Condens. Matter*, vol. 24, p. 345601, 2012.
- [18] P. Coleman, "Theories of non-Fermi liquid behavior in heavy fermions," *Phys. B Condens. Matter*, vol. 259, pp. 353–358, 1999.
- [19] L. Hozoi, H. Gretarsson, J. P. Clancy, B. G. Jeon, B. Lee, K. H. Kim, V. Yushankhai, P. Fulde, Y. J. Kim, and J. van den Brink, "Topological states in pyrochlore iridates: long-range anisotropy strongly competing with spin-orbit interaction," *ArXiv e-prints*, 2012.
- [20] J. P. Clancy, N. Chen, C. Y. Kim, W. F. Chen, K. W. Plumb, B. C. Jeon, T. W. Noh, and Y. Kim, "Spin-orbit coupling in iridium-based 5 d compounds probed by x-ray absorption spectroscopy," *Phys. Rev. B*, vol. 86, no. 19, pp. 1–8, 2012.
- [21] S. Blundell and D. Thouless, *Magnetism in condensed matter. Vol. 18*. Oxford: Oxford university press, 2001.
- [22] Y. Takikawa, S. Ebisu, and S. Nagata, "Van Vleck paramagnetism of the trivalent Eu ions," *J. Phys. Chem. Solids*, vol. 71, pp. 1592–1598, 2010.
- [23] K. Gatterer and H. P. Fritzer, "Magnetic susceptibility of the Van Vleck paramagnet $Cs_5Eu(N_3)_8$," *J. Phys. Condens. Matter*, vol. 4, pp. 4667–4673, 1992.
- [24] P. Dasgupta, Y. M. Jana, a. Nag Chattopadhyay, R. Higashinaka, Y. Maeno, and D. Ghosh, "Low-temperature measurements of magnetic susceptibility and specific heat of $Eu_2Ti_2O_7$ -An XY pyrochlore," *J. Phys. Chem. Solids*, vol. 68, no. 3, pp. 347–354, 2007.
- [25] M. Tovar, D. Rao, J. Barnett, S. B. Oseroff, J. D. Thompson, S.-W. Cheong, Z. Fisk, D. C. Vier, and S. Schultz, "Eu₂CuO₄: An anisotropic van Vleck Paramagnet," *Phys. Rev. B*, vol. 39, no. 4, pp. 2661–2663, 1989.
- [26] S. T. Bramwell, M. J. Harris, B. C. den Hertog, M. J. Gingras, J. S. Gardner, D. F. McMorrow, a R. Wildes, a L. Cornelius, J. D. Champion, R. G. Melko, and T. Fennell, "Spin correlations in $Ho_2Ti_2O_7$: a dipolar spin ice system.," *Phys. Rev. Lett.*, vol. 87, p. 047205, 2001.
- [27] J. Snyder, J. S. Slusky, R. J. Cava, and P. Schiffer, "How 'spin ice' freezes," *Nature*, vol. 413, no. 6851, pp. 48–51, 2001.
- [28] M. J. P. Gingras, "Physics. Observing monopoles in a magnetic analog of ice.," *Science*, vol. 326, pp. 375–376, 2009.

- [29] W. Witczak-Krempa, G. Chen, Y. B. Kim, and L. Balents, "Correlated Quantum Phenomena in the Strong Spin-Orbit Regime," *Annu. Rev. Condens. Matter Phys.*, vol. 5, pp. 57–82, 2014.
- [30] X. Ou and H. Wu, "Impact of spin-orbit coupling on the magnetism of Sr₃MIrO₆ (M = Ni, Co)," *Sci. Rep.*, vol. 4, 2014.
- [31] B. J. Kim, H. Jin, S. J. Moon, J. Y. Kim, B. G. Park, C. S. Leem, J. Yu, T. W. Noh, C. Kim, S. J. Oh, J. H. Park, V. Durairaj, G. Cao, and E. Rotenberg, "Novel $j=1/2$ mott state induced by relativistic spin-orbit coupling in Sr₂IrO₄," *Phys. Rev. Lett.*, vol. 101, no. August, pp. 1–4, 2008.
- [32] A. R. West, *Solid State Chemistry And Its Applications*, Second Edi. 2007.
- [33] B. Hafner, "Scanning Electron Microscopy Primer," *Charact. Facil. Univ. Minnesota—Twin Cities*, pp. 1–29, 2007.
- [34] Quantum Design, "Quantum Design Hardware Manual," no. 1070–002 R, pp. 1–8.
- [35] QuantumDesign, "MPMS Technical Note 1014-210." pp. 1–8, 1997.
- [36] T. J. B. Holland, S. A. T. Redfern, and D. Street, "Unit cell refinement from powder diffraction data : the use of regression diagnostics," *Mineral. Mag.*, vol. 61, no. February, pp. 65–77, 1997.
- [37] N. Aito, M. Soda, Y. Kobayashi, and M. Sato, "Spin- Glass like Transition and Hall Resistivity of Y_{2-x}BixIr₂O₇," *J. Phys. Soc. Japan*, vol. 72, no. 5, pp. 1226–1230, 2003.
- [38] B. P. Mandal and a. K. Tyagi, "Preparation and high temperature-XRD studies on a pyrochlore series with the general composition Gd_{2-x}NdxZr₂O₇," *J. Alloys Compd.*, vol. 437, pp. 260–263, 2007.
- [39] B. J. Kennedy, "Structural Trends in Pyrochlore Oxides," *Mater. Sci. Forum*, vol. 228–231, no. 1998, pp. 753–758, 1996.
- [40] J. N. Millican, R. T. Macaluso, S. Nakatsuji, Y. Machida, Y. Maeno, and J. Y. Chan, "Crystal growth and structure of R₂Ir₂O₇ (R = Pr, Eu) using molten KF," *Mater. Res. Bull.*, vol. 42, pp. 928–934, 2007.
- [41] AMETEK, "EDAX Periodic Table." AMETEK Materials Analysis Division.
- [42] N. Taira, M. Wakeshima, and Y. Hinatsu, "Magnetic properties of iridium pyrochlores R₂Ir₂O₇ (R= Y, Sm, Eu and Lu)," *J. Phys. Condens. Matter*, vol. 13, p. 5527, 2001.
- [43] W. K. Zhu, M. Wang, B. Seradjeh, F. Yang, and S. X. Zhang, "Enhanced weak ferromagnetism and conductivity in hole-doped pyrochlore iridate Y₂Ir₂O₇," *Phys. Rev. B*, vol. 90, pp. 1–7, 2014.
- [44] K. Blacklock and H. W. White, "Specific heats of the pyrochlore compounds Eu₂Ir₂O₇ and Lu₂Ir₂O₇," *J. Chem. Phys.*, vol. 72, no. 1980, p. 2191, 1980.

- [45] www.knowledgedoor.com, "Electronic Heat Capacity Coefficient The Elements Handbook." .
- [46] C. Kittel, *Introduction to solid state physics*. 2005.
- [47] K. P. Sinha and N. Kumar, *Interactions in Magnetically Ordered Solids*. Oxford University Press, 1980.
- [48] S. Saha, S. Singh, B. Dkhil, S. Dhar, R. Suryanarayanan, G. Dhalenne, A. Revcolevschi, and A. K. Sood, "Temperature dependent Raman and x-ray studies of spin-ice pyrochlore Dy₂Ti₂O₇ and non-magnetic pyrochlore Lu₂Ti₂O₇," *Phys. Rev. B - Condens. Matter Mater. Phys.*, vol. 78, no. 21, p. 214102, 2008.
- [49] N. Taira, M. Wakeshima, and Y. Hinatsu, "Magnetic susceptibility and specific heat studies on heavy rare earth ruthenate pyrochlores R₂Ru₂O₇ (R = Gd–Yb)," *J. Mater. Chem.*, vol. 12, no. 5, pp. 1475–1479, 2002.
- [50] N. P. Raju, E. Gmelin, and R. K. Kremer, "Magnetic Susceptibility and Specific Heat Studies of Spin-glass-like ordering in the pyrochlore compounds R₂Mo₂O₇ (R = Y, Sm, or Gd)," *Phys. Rev. B*, vol. 46, no. 9, pp. 5405–5411, 1992.
- [51] S. Singh, S. Saha, S. K. Dhar, R. Suryanarayanan, a. K. Sood, and A. Revcolevschi, "Manifestation of geometric frustration on magnetic and thermodynamic properties of the pyrochlores Sm₂X₂O₇ (X=Ti,Zr)," *Phys. Rev. B - Condens. Matter Mater. Phys.*, vol. 77, no. 5, p. 054408, 2008.
- [52] M. Soda, N. Aito, Y. Kurahashi, Y. Kobayashi, and M. Sato, "Transport, thermal and magnetic properties of pyrochlore oxides y 2-xBixIr₂O₇," *Phys. B Condens. Matter*, vol. 329–333, pp. 1071–1073, 2003.
- [53] M. J. Graf, S. M. Disseler, C. Dhital, T. Hogan, M. Bojko, a Amato, H. Luetkens, C. Baines, D. Margineda, S. R. Giblin, M. Jura, and S. D. Wilson, "Effect of carrier concentration on magnetism and magnetic order in the pyrochlore iridates," *arXiv.org*, vol. cond-mat.s, 2014.
- [54] F. F. Tafti, J. J. Ishikawa, a. McCollam, S. Nakatsuji, and S. R. Julian, "Pressure-tuned insulator to metal transition in Eu₂Ir₂O₇," *Phys. Rev. B - Condens. Matter Mater. Phys.*, vol. 85, pp. 1–7, 2012.